



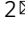





# Kinesin-8-specific loop-2 controls the dual activities of the motor domain according to tubulin protofilament shape

Byron Hunter<sup>1,4</sup>, Matthieu P. M. H. Benoit <sup>2,4</sup>, Ana B. Asenjo <sup>2</sup>, Caitlin Doubleday<sup>1</sup>, Daria Trofimova<sup>1</sup>, Corey Frazer <sup>3</sup>, Irsa Shoukat<sup>1</sup>, Hernando Sosa <sup>2</sup>  & John S. Allingham <sup>1</sup> 

Kinesin-8s are dual-activity motor proteins that can move processively on microtubules and depolymerize microtubule plus-ends, but their mechanism of combining these distinct activities remains unclear. We addressed this by obtaining cryo-EM structures (2.6–3.9 Å) of *Candida albicans* Kip3 in different catalytic states on the microtubule lattice and on a curved microtubule end mimic. We also determined a crystal structure of microtubule-unbound CaKip3-ADP (2.0 Å) and analyzed the biochemical activity of CaKip3 and kinesin-1 mutants. These data reveal that the microtubule depolymerization activity of kinesin-8 originates from conformational changes of its motor core that are amplified by dynamic contacts between its extended loop-2 and tubulin. On curved microtubule ends, loop-1 inserts into preceding motor domains, forming head-to-tail arrays of kinesin-8s that complement loop-2 contacts with curved tubulin and assist depolymerization. On straight tubulin protofilaments in the microtubule lattice, loop-2-tubulin contacts inhibit conformational changes in the motor core, but in the ADP-Pi state these contacts are relaxed, allowing neck-linker docking for motility. We propose that these tubulin shape-induced alternations between pro-microtubule-depolymerization and pro-motility kinesin states, regulated by loop-2, are the key to the dual activity of kinesin-8 motors.

<sup>1</sup>Department of Biomedical and Molecular Sciences, Queen's University, Kingston, ON K7L 3N6, Canada. <sup>2</sup>Department of Biochemistry, Albert Einstein College of Medicine, Bronx, NY 10461, USA. <sup>3</sup>Department of Molecular Microbiology and Immunology, Brown University, Providence, RI 02912, USA. <sup>4</sup>These authors contributed equally: Byron Hunter, Matthieu P. M. H. Benoit. email: [hernando.sosa@einsteinmed.edu](mailto:hernando.sosa@einsteinmed.edu); [allinghj@queensu.ca](mailto:allinghj@queensu.ca)

Members of the kinesin-8 family are unique, as they often integrate the two enzymatic activities of processive microtubule plus-end-directed motility and microtubule depolymerization into a single ~40 kDa motor domain<sup>1–7</sup>. These activities allow kinesin-8s to localize to the ends of cytoplasmic or spindle microtubules, where they can regulate mitotic spindle size, spindle position, and chromosomal congression<sup>5,8–16</sup>. In many eukaryotes in which these motor proteins have been studied, the motile and depolymerization activities are produced by their N-terminal motor domain, while their C-terminal tail has an additional microtubule-binding site that helps regulate the functions of the motor domain<sup>5,17–19</sup>. A lack of high-resolution structures capturing a kinesin-8 motor domain at each major step of its motile and microtubule depolymerization cycles has limited our understanding of the relationship between these two catalytic cycles and the structural elements of the motor domain that control them.

At this time, our knowledge of the catalytic cycles of kinesins is limited to motile kinesins that are incapable of microtubule depolymerization, and to microtubule-depolymerizing kinesins that are non-motile. In motile kinesins, such as kinesin-1 and kinesin-3, microtubule lattice binding by one of their two motor domains opens the nucleotide-binding pocket, allowing ADP release<sup>20–22</sup>. Subsequent entry of ATP initiates closing of the nucleotide-binding pocket and docking of a short peptide, known as the neck-linker, along the side of the motor domain. Neck-linker docking in the microtubule-bound motor domain propels the second, microtubule-unbound, motor domain towards the microtubule plus-end, enabling a single stepping event. In the non-motile microtubule-depolymerizing kinesin-13s, which move on microtubules by diffusion<sup>23</sup>, ATP binding does not induce closure of the nucleotide-binding pocket on the microtubule lattice<sup>24</sup>. Only when kinesin-13 is bound to curved  $\alpha\beta$ -tubulin protofilaments found at microtubule ends does the nucleotide-binding pocket close in the presence of ATP<sup>24,25</sup>. In this case, closing the nucleotide-binding pocket allows kinesin-13-specific structural elements to promote further tubulin bending, leading to microtubule depolymerization<sup>26,27</sup>. The motility and depolymerization cycles in purely motile and purely depolymerizing kinesins are thus very different. The features of the kinesin-8 cycle that allow their motors to combine both activities remain unknown.

An important gap in our understanding of the kinesin-8 depolymerization mechanism is the lack of a kinesin-8 structure bound to curved tubulin. Functional studies of *Saccharomyces cerevisiae* kinesin-8 Kip3 (ScKip3) have proposed that upon reaching the curved conformation of tubulin at the plus-end, the motor domain experiences a conformational switch that suppresses ATP hydrolysis<sup>28</sup>. As a result, prolonged, tight interactions between kinesin-8 and the microtubule plus-end stabilize protofilament curvature and promote microtubule depolymerization. The suggested mechanism for this tubulin shape-dependent ATPase switch involves formation of an interaction between loop-11 of the motor domain and an aspartate residue on helix-3 of  $\alpha$ -tubulin (Asp118—yeast tubulin, Asp116—bovine or porcine tubulin). Subsequent molecular dynamics studies identified an arginine within loop-11 (Arg351—ScKip3) as a potential candidate residue that interacts with  $\alpha$ -tubulin Asp118/116 in the curved conformation<sup>29</sup>. Studies on the human kinesin-8s KIF18A and KIF19A have also implicated separate regions of the microtubule-binding interface, namely loop-2 and loop-8, as elements that are likely involved in stabilizing curved tubulin protofilaments<sup>30–32</sup>. Ultimately, a structure of a kinesin-8 motor bound to curved tubulin is needed to elucidate how discrete parts of the motor domain contribute to kinesin-8-mediated microtubule depolymerization.

Mechanistically, it is well-established that some kinesin-8s operate cooperatively to induce microtubule depolymerization<sup>2,3,18,28</sup>. Both in vitro and in vivo, a build-up of motors at the plus-end is required for effective disassembly of microtubule polymers. As longer microtubules accumulate more motors than shorter microtubules, longer microtubules are depolymerized faster—an effect termed length-dependent depolymerization. The structural basis underlying this cooperative length-dependent microtubule depolymerization is not understood. It is also not clear if and how kinesin-8s physically interact to collectively produce forces needed to dissociate tubulin dimers.

To understand the mechanistic basis for the dual-functionality of kinesin-8, we obtained seven cryo-EM structures of *Candida albicans* Kip3 bound to either the microtubule lattice or curved microtubule end mimics, and a microtubule-unbound CaKip3 X-ray structure. We also performed biochemical experiments on CaKip3 and human kinesin-1 constructs with their loop-2 region swapped or loop-1 region truncated. On straight protofilaments within the central microtubule lattice, we observed that loop-2 forms extensive contacts with  $\alpha$ -tubulin that temporarily restrict the ATP-bound motor in a non-motile, open conformation. Only in the post-ATP-hydrolysis state of microtubule-bound CaKip3 are the loop-2-tubulin interactions relaxed enough to allow nucleotide-binding pocket closure and neck-linker docking, producing a pro-motility state. On curved protofilaments, we observe that loop-2 retracts and promotes closing of the nucleotide-binding pocket around ATP, while loop-1 inserts into the preceding motor domain, forming a pro-depolymerization state. When we replaced CaKip3's loop-2 with the short loop-2 of kinesin-1, and truncated loop-1, the microtubule depolymerization activity of CaKip3 decreased substantially. Alternatively, swapping loop-2 from kinesin-1 into CaKip3 increased the microtubule-stimulated ATPase and microtubule-gliding speed of CaKip3. These findings show that the kinesin-8-specific extended loop-2 is a central element that coordinates the motility and depolymerase activities of kinesin-8 in accord with the shape of tubulin it binds and that CaKip3's microtubule depolymerization activity involves loop-2-amplified conformational changes of its motor domain and inter-motor domain contacts through loop-1. We also show that the unconventional conformations of CaKip3's ATPase cycle on microtubules, modulated by loop-2, bear several similarities to kinesin-13s<sup>24</sup>.

## Results

**Structures of CaKip3 reveal a unique ATPase cycle.** The pathogenic yeast *Candida albicans* expresses a single kinesin-8 homolog, dubbed CaKip3, whose motor domain shares 60% sequence identity with that of *S. cerevisiae* Kip3 (Supplementary Fig. 1a). *C. albicans* cells lacking this protein exhibit striking growth defects that are indicative of cell cycle arrest and are unable to form hyphae under conditions that induce filamentous growth (Supplementary Fig. 2a–d)<sup>33</sup>. Similar to observations in other eukaryotes<sup>3,9,10,15,17,34–41</sup>, loss of kinesin-8 activity in *C. albicans* produces unusually long and more numerous astral microtubules, long mitotic spindles with a “fishhook” morphology, and delays in the timing of anaphase entry (Supplementary Fig. 2e–j)<sup>42</sup>. These effects of CaKip3 loss are consistent with a functional role in nuclear positioning and chromosome segregation by regulating microtubule length. We therefore used CaKip3 as a model to understand the molecular mechanisms of motility and microtubule depolymerization by kinesin-8s.

We solved high-resolution structures of the CaKip3 motor domain at key intermediates in its motile cycle, as well as its structure on curved  $\alpha\beta$ -tubulin rings that mimic protofilaments at a depolymerizing microtubule plus-end (Fig. 1). To visualize the

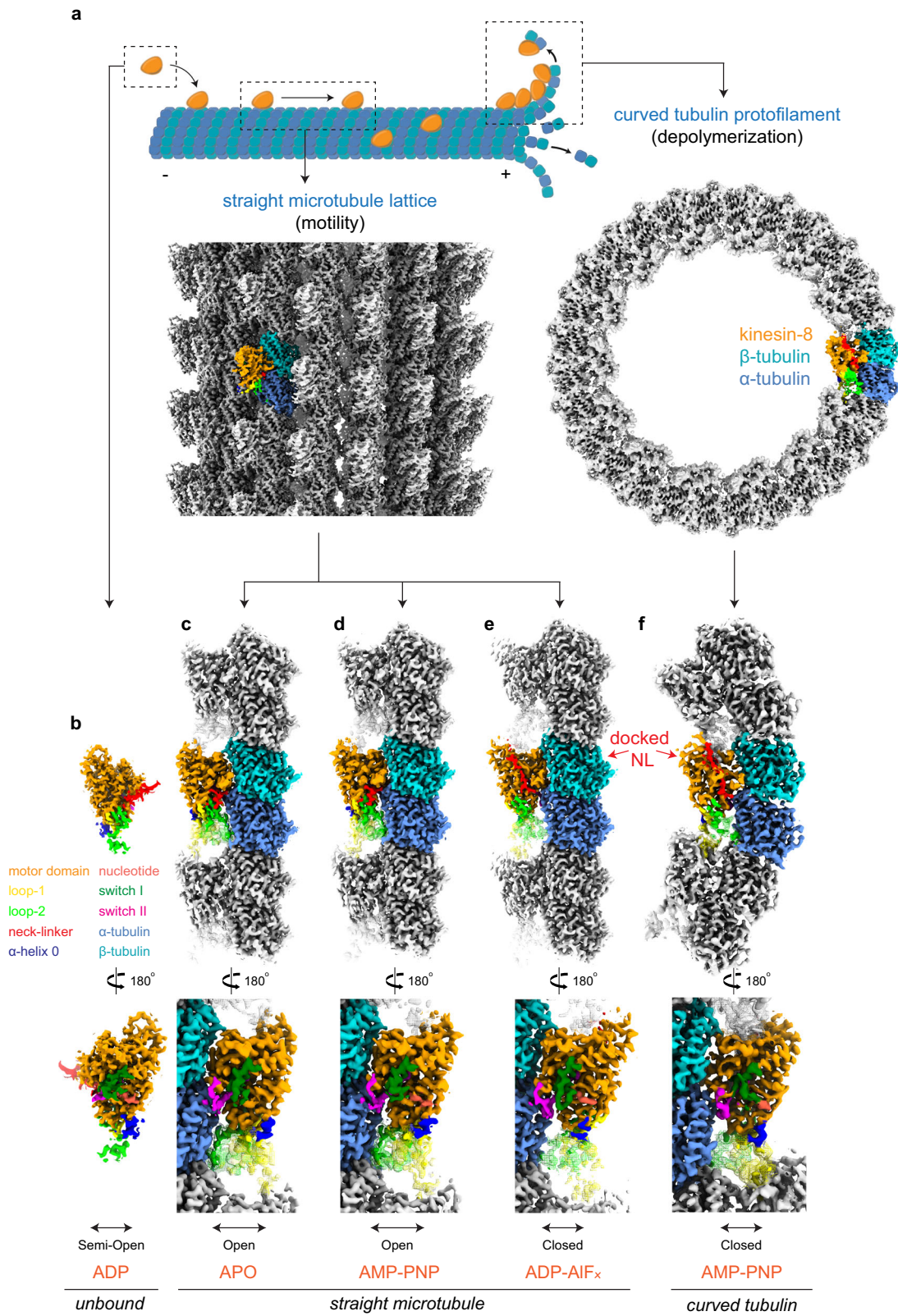


**Fig. 1 Structures of microtubule-unbound, microtubule-bound, and curved tubulin-bound CaKip3.** **a** Top—Cartoon representation of catalytic intermediates of CaKip3’s motility and microtubule depolymerization cycles. Bottom—Example of a CaKip3-decorated microtubule (MT-CaKip3-MDC-ANP) cryo-EM map and the full CaKip3-decorated dolastatin-tubulin-ring cryo-EM map. **b** X-ray crystallographic density of CaKip3-MDN in the ADP state. **c–e** Cryo-EM maps of microtubule-bound CaKip3-MDC in the APO, AMP-PNP, and ADP-AIF<sub>x</sub> nucleotide states. **f** Cryo-EM maps of curved tubulin-bound CaKip3-MDC in the AMP-PNP state. Map surfaces are colored regionally according to the segment of the fitted protein model they enclose: α-tubulin (cornflower blue), β-tubulin (sky blue), kinesin motor core (orange), Switch I loop (forest green), loop-11 of Switch II (magenta), neck-linker (red), nucleotide (tomato), loop-1 (yellow), loop-2 (lime green), helix-0 (dark blue). The figure was prepared with UCSF ChimeraX<sup>87</sup>.

**Table 1 X-ray diffraction data collection, refinement, and validation statistics.**

	<b>CaKip3-MDN-ADP (PDB 7LFF)</b>
Data collection	
Wavelength	0.9795
Resolution range (Å)	45.91–2.01 (2.08–2.01)
Space group	P1
Unit-cell	
<i>a</i> , <i>b</i> , <i>c</i> (Å)	43.99, 52.68, 86.75
$\alpha$ , $\beta$ , $\gamma$ (°)	86.9, 79.996, 89.924
Unique reflections	49650 (4913)
Multiplicity	2.7 (2.69)
Completeness (%)	97.09 (96.7)
Average <i>I</i> / $\sigma$ ( <i>I</i> )	4.6 (0.3)
Average CC1/2	0.995 (0.149)
Wilson B-factor (Å <sup>2</sup> )	46.5
<i>R</i> <sub>merge</sub> (%)	11.4
<i>R</i> <sub>pim</sub> (%)	8.2
<i>R</i> <sub>meas</sub> (%)	14.1
Structure refinement	
No. of reflections	49471 (4807)
Completeness (%)	97.1 (92.79)
<i>R</i> <sub>work</sub> for 95% data (%)	23.23 (48.59)
<i>R</i> <sub>free</sub> for 5% data (%)	26.76 (51.13)
RMSD bond lengths (Å)	0.0049
RMSD bond angles (°)	1.0467
<i>B</i> <sub>ave</sub> (Å <sup>2</sup> )/protein atoms	60.07/5273
<i>B</i> <sub>ave</sub> (Å <sup>2</sup> )/ligand atoms	46.37/56
<i>B</i> <sub>ave</sub> (Å <sup>2</sup> )/water molecules	53.09/142
Ramachandran favored (%)	95.05
Ramachandran allowed (%)	3.86
Ramachandran outliers (%)	1.08

Statistics for the highest-resolution shell are shown in parentheses.

microtubule-unbound ADP state of *CaKip3*, we determined a 2.0 Å X-ray crystal structure of a construct containing the motor domain and a slightly truncated neck-linker (*CaKip3*-MDN, residues 1–436) (Fig. 1b and Supplementary Fig. 1b). Using a longer *CaKip3* construct containing the motor domain, neck-linker, and the first predicted coiled-coil-forming domain (*CaKip3*-MDC, residues 1–482) (Supplementary Fig. 1b), we obtained 2.6–3.3 Å (Supplementary Fig. 3) cryo-electron microscopy (cryo-EM) structures of microtubule-bound *CaKip3* in: (1) a nucleotide-free state (Fig. 1c), (2) an ATP-like state using the non-hydrolysable ATP analog AMP-PNP (Fig. 1d), and (3) an ADP-Pi-like transition state using ADP- $\text{AlF}_x$  (Fig. 1e). To view *CaKip3*'s interactions with curved  $\alpha\beta$ -tubulin protofilaments, we obtained a 3.9 Å cryo-EM structure of *CaKip3*-MDC bound to dolastatin-stabilized curved tubulin rings and AMP-PNP (Fig. 1f and Supplementary Fig. 4)<sup>43</sup>. The data processing and model refinement statistics for the X-ray crystal structure and all cryo-EM structures are reported in Tables 1 and 2, respectively.

Comparing the different *CaKip3* structures reveals that the conformational changes experienced by the kinesin-8 motor domain core during microtubule binding in relation to its ATP hydrolysis cycle are different from purely motile kinesins. The *CaKip3*-MDN-ADP crystal structure has a partially open nucleotide pocket and an undocked neck-linker (Fig. 1b and Supplementary Figs. 5 and 6). The Switch I region (loop-9) is well-defined but angled away from ADP, while the Switch II region (loop-11) that coordinates microtubule sensing and nucleotide binding is mostly disordered. When *CaKip3*-MDC binds the microtubule (MT-*CaKip3*-MDC-APO), the minus subdomain rotates relative to the plus subdomain, opening the nucleotide-binding pocket further (Figs. 1c and 2a;

Supplementary Movie 1). Here, the full length of loop-11 is visible and interacts with helices 3', 3, 11', and 12 of  $\alpha$ -tubulin (Supplementary Fig. 12a). Unexpectedly, binding of ATP to the MT-*CaKip3*-MDC complex, as mimicked by AMP-PNP, fails to induce a “pro-motility” conformational change (i.e., nucleotide-binding pocket closure and neck-linker docking on the microtubule lattice) even though the *CaKip3*-MDC construct includes the full neck-linker (Figs. 1d and 2b; Supplementary Figs. 6 and 7, Supplementary Movie 1). The cryo-EM map of the MT-*CaKip3*-MDC-ANP complex clearly shows that the nucleotide-binding pocket is open, and the neck-linker is undocked, similar to MT-*CaKip3*-MDC-APO (compare Fig. 1c, d). This is striking because all microtubule-bound structures of motile kinesins with a full neck-linker that is not pulled backward by a trailing head exhibit a closed nucleotide-binding pocket in the ATP-bound state (as mimicked by AMP-PNP) (compare Supplementary Fig. 7b, c, and i)<sup>21,44–46</sup>. In this regard, *CaKip3* is more akin to depolymerizing kinesins than to motile kinesins<sup>24</sup>. Only in the post-ATP-hydrolysis state (MT-*CaKip3*-MDC-AAF) does the microtubule-bound *CaKip3* motor domain adopt the pro-motility conformation with a closed nucleotide-binding pocket and docked neck-linker, allowing *CaKip3* to complete its motile cycle (Figs. 1e and 2c; Supplementary Fig. 3b, Supplementary Movie 1).

Our library of structures defines the subdomain motions associated with nucleotide-binding pocket closure in *CaKip3*. When the nucleotide-binding pocket closes in the MT-*CaKip3*-MDC-AAF complex, the minus subdomain has a strong rotational component in the plane perpendicular to the microtubule axis (Fig. 2c and Supplementary Movie 1). We observe these same conformational changes in *CaKip3*-MDC when it is bound to curved tubulin rings and AMP-PNP (CT-*CaKip3*-MDC-ANP) (Fig. 2d and Supplementary Movie 1). When viewed from the microtubule minus end, it is evident that closure of the nucleotide-binding pocket is associated with a counter-clockwise rotation of the minus subdomain and a clockwise rotation of the Switch I and II regions (Fig. 2c, d; left panels, Supplementary Movie 1). Movement of these subdomains in the plane parallel to the microtubule axis results in a relative displacement of the tubulin-interacting regions to better fit curved tubulin, which is similar overall to what was reported in kinesin-13 (Supplementary Fig. 7h)<sup>24</sup>. In the MT-*CaKip3*-MDC-AAF and CT-*CaKip3*-MDC-ANP complexes, the displacement of tubulin-interacting regions relative to  $\beta$ -tubulin is greatest at the kinesin-8-specific elongated loop-2 that extends the kinesin-tubulin interface (Fig. 2c, d; right panels, Supplementary Movie 1). Prominent as well is movement of the loop-8 lobe toward helix-12 of  $\beta$ -tubulin. Unexpectedly, we also observe a small rotation of  $\alpha$ -tubulin relative to  $\beta$ -tubulin in the MT-*CaKip3*-MDC-AAF complex, giving a slight outward curvature to each *CaKip3*-bound  $\alpha\beta$ -tubulin subunit in the microtubule lattice when the nucleotide-binding pocket of *CaKip3* is closed (Fig. 2c; right panels—blue arrows on  $\alpha$ -tubulin, Supplementary Movie 1).

**Extensive and variable loop-2 contacts with  $\alpha$ -tubulin.** Collectively, our *CaKip3* structural data shows well-defined map density for the lengthy loop-2 region that extends out of the  $\beta$ 1b/ $\beta$ 1c strands, toward the minus end of the microtubule. The electron density from the *CaKip3*-MDN-ADP crystal allowed us to model residues Phe116 to Ala131 of loop-2, which includes a proline-rich region and a ~10-residue helical sequence that is shared by some kinesin-8s (Fig. 3a and Supplementary Fig. 1a). The cryo-EM maps of MT-*CaKip3*-MDC-APO and MT-*CaKip3*-MDC-ANP show that the section of loop-2 that precedes the  $\beta$ 1c strand, which is not resolved in the X-ray structure, becomes ordered on the microtubule while *CaKip3* is in the open conformation

**Table 2 Cryo-EM data collection, refinement, and validation statistics (1/2).**

	<b>MT-CaKip3-MDC AMP-PNP (EMDB-26074) (PDB 7TQX)</b>	<b>MT-CaKip3-MDC ADP-AIF<sub>x</sub> (EMDB-26075) (PDB 7TQY)</b>	<b>MT-CaKip3-MDC APO (EMDB-26076) (PDB 7TQZ)</b>	<b>MT-CaKip3-MDN AMP-PNP (EMDB-26077) (PDB 7TR0)</b>
<b>Data collection and processing</b>				
Magnification (actual)	60,606	58,893	60,606	60,241
Voltage (kV)	300	300	300	300
Electron exposure (e <sup>-</sup> /Å <sup>2</sup> )	70.4	63.3	71.1	69.6
Defocus range (µm) <sup>a</sup>	-0.8; -2.1	-0.8; -1.7	-0.9; -1.8	-0.9; -1.7
Pixel size (Å)	0.825	0.849	0.825	0.830
Symmetry imposed <sup>b</sup>	Helical	Helical	Helical	Helical
Rise (Å)	5.56	5.44	5.55	5.56
Twist (deg)	168.09	168.07	168.09	168.09
Particle images identified as 15R symmetry (no.)	12,120	23,783	16,061	77,728
Particle images in helical reconstruction (no.)	12,120	23,783	16,061	77,728
Single particles (no.) <sup>c</sup>	181,800	356,745	240,915	1,165,920
Single particles used (no.) <sup>d</sup>	124,055	255,526	162,955	501,258
Overall resolution (Å)	2.8	2.6	2.7	2.7
FSC threshold	0.143	0.143	0.143	0.143
Kinesin resolution (Å)	3.1	2.9	3.0	2.9
Tubulin resolution (Å)	2.8	2.6	2.7	2.7
<b>Refinement</b>				
<b>Model composition</b>				
Non-hydrogen atoms	9824	9892	9791	9836
Protein residues	1229	1235	1229	1229
Ligands	6	7	4	5
<b>R.m.s. deviations</b>				
Bond lengths (Å)	0.0054	0.0054	0.0061	0.0058
Bond angles (°)	1.14	1.17	1.19	1.17
<b>Validation</b>				
MolProbity score	1.48	1.36	1.48	1.36
Clashscore	4.28	3.23	5.01	4.27
Poor rotamers (%)	0.47	1.12	0.94	0.66
<b>Ramachandran plot</b>				
Favored (%)	96.07	96.66	96.64	97.13
Allowed (%)	3.93	3.34	3.36	2.87
Disallowed (%)	0.00	0.00	0.00	0.00
	<b>MT-CaKip3-MDN<sub>L2-HsKHC</sub> AMP-PNP (EMDB-26078) (PDB 7TR1)</b>	<b>MT-CaKip3-MDN<sub>L2-HsKHC</sub> APO (EMDB-26079) (PDB 7TR2)</b>	<b>CT-CaKip3-MDC AMP-PNP (EMDB-26080) (PDB 7TR3)</b>	
<b>Data collection and processing</b>				
Magnification (actual)	45,872	58,893	46,168	
Voltage (kV)	300	300	300	
Electron exposure (e <sup>-</sup> /Å <sup>2</sup> )	64.0	64.6	64.0	
Defocus range (µm) <sup>a</sup>	-0.8; -1.9	-0.8; -1.7	-0.9; -3.2	
Pixel size (Å)	1.090	0.849	1.083	
Symmetry imposed <sup>b</sup>	Helical	Helical	C14	
Rise (Å)	5.54	5.55		
Twist (deg)	168.08	168.09		
Particle images identified as 15R/C14 symmetry (no.)	37,146	12,219	37,920	
Particle images in helical/C14 reconstruction (no.)	37,146	12,219	37,920	
Single particles (no.) <sup>c</sup>	557,190	183,285	530,936	
Single particles used (no.) <sup>d</sup>	67,238	98,446	530,936	
Overall resolution (Å)	3.1	3.0	3.9	
FSC threshold	0.143	0.143	0.143	
Kinesin resolution (Å)	3.4	3.4	3.9	
Tubulin resolution (Å)	3.0	3.0	3.9	
<b>Refinement</b>				
<b>Model composition</b>				
Non-hydrogen atoms	9708	9588	10,224	
Protein residues	1216	1207	1289	
Ligands	6	4	4	

**Table 2 (continued)**

	<b>MT-CaKip3-MDN<sub>L2-HsKHC</sub> AMP-PNP (EMDB-26078) (PDB 7TR1)</b>	<b>MT-CaKip3-MDN<sub>L2-HsKHC</sub> APO (EMDB-26079) (PDB 7TR2)</b>	<b>CT-CaKip3-MDC AMP-PNP (EMDB-26080) (PDB 7TR3)</b>
R.m.s. deviations			
Bond lengths (Å)	0.0055	0.0055	0.0053
Bond angles (°)	1.14	1.15	1.13
Validation			
MolProbity score	1.44	1.37	1.90
Clashscore	3.39	3.11	7.04
Poor rotamers (%)	0.19	1.05	0.36
Ramachandran plot			
Favored (%)	95.61	96.33	91.26
Allowed (%)	4.39	3.67	8.50
Disallowed (%)	0.00	0.00	0.23

<sup>a</sup>Range of the per-particle defocus estimates. The range corresponds to 90% of the particles used, 5% of the particle defocusses are below and 5% are above this range.

<sup>b</sup>Symmetry imposed during the symmetrical refinement done before the local refinements (rise and twists provided for helical symmetry only).

<sup>c</sup>Total number of particles after symmetry expansion.

<sup>d</sup>Number of asymmetric units, corresponding to a kinesin motor bound to a tubulin dimer, used after 3D classification.

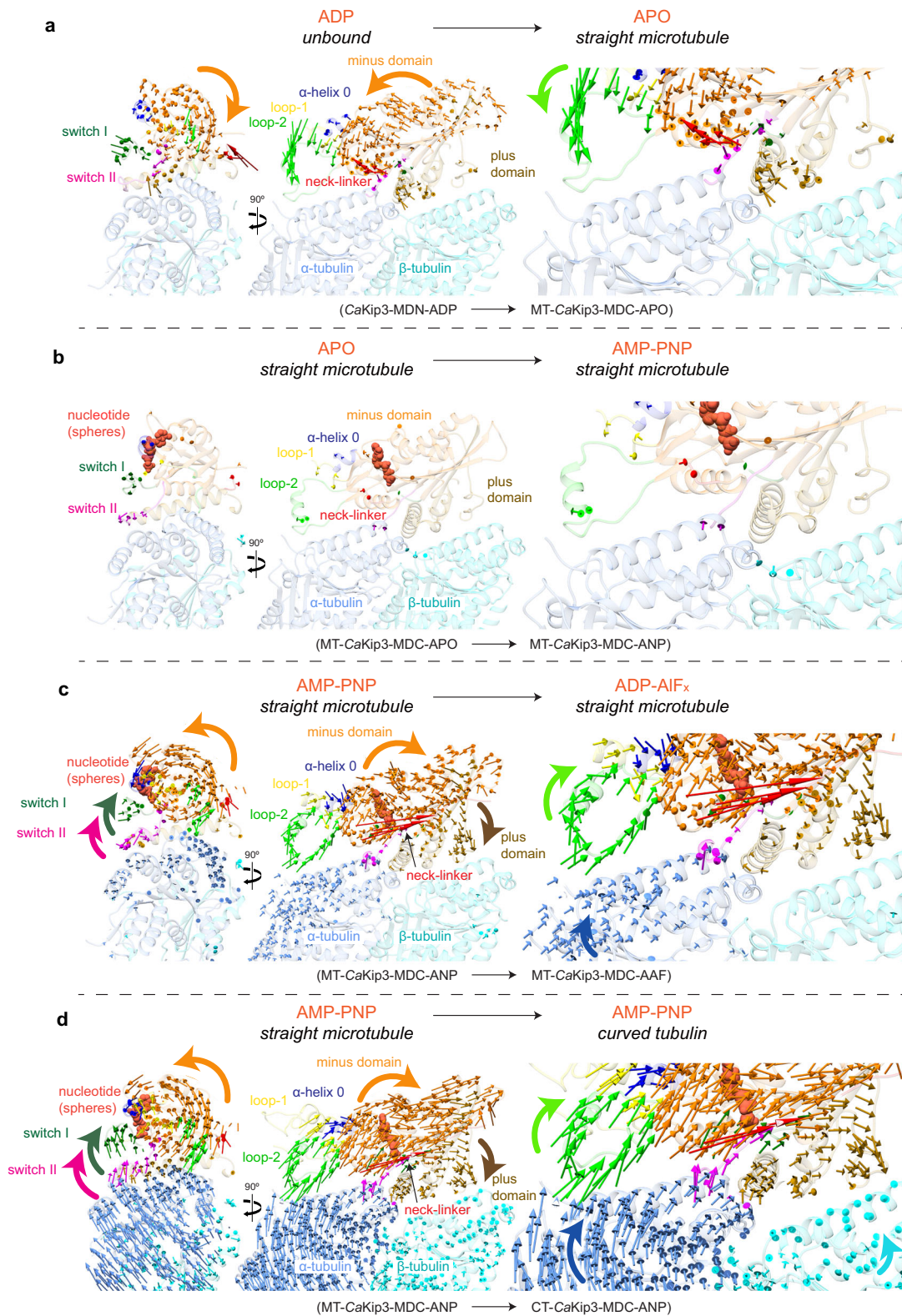
(Fig. 3c, d; left panels). This section interacts with helix-12 and a loop between helix-7 and the  $\beta 7$  strand of  $\alpha$ -tubulin via residues Phe136, Ser139, Arg140, and one of the two visible conformations of the side chain of His144 (Fig. 3c, d; right panels). These loop-2-tubulin interactions are more numerous than the loop-2 contacts made by kinesin-13s<sup>24</sup>, which are essential for kinesin-13's microtubule depolymerization activity<sup>24,26,27,47–49</sup>. Several of the CaKip3 loop-2-tubulin helix-12 interactions are electrostatic. For example, Arg140 is close enough to  $\alpha$ -tubulin to hydrogen bond with Glu420 and Asp424 in helix-12. These contacts confirm earlier assumptions that loop-2 contributes positively charged residues that associate with the negatively charged surface of  $\alpha$ -tubulin<sup>31</sup>. We observe similar loop-2-tubulin contacts, and overall motor domain conformation in the two microtubule-bound AMP-PNP structures, MT-CaKip3-MDC-ANP and MT-CaKip3-MDN-ANP (Fig. 4c).

In the MT-CaKip3-MDC-AAF and CT-CaKip3-MDC-ANP complexes, the loop-2 density is much weaker, indicating a more mobile loop structure. We could trace the average path of loop-2 in these complexes by applying a low-pass filter of 9 and 7 Å, respectively (Fig. 3e, f; left panels). In CT-CaKip3-MDC-ANP, stronger density is visible along  $\alpha$ -tubulin, especially near the loop-2 tip around  $\alpha$ -tubulin residue Y262, compared to MT-CaKip3-MDC-AAF, indicating MT-CaKip3-MDC-AAF has the most mobile loop-2. In both complexes, much of loop-2 is shifted away from helix-12 of  $\alpha$ -tubulin to a degree that many of the bonds observed in the APO and AMP-PNP states would not form (Fig. 3e, f; right panels). These changes in the conformation of loop-2 are accompanied by movement of the  $\beta 1$  strand and helix-6 of CaKip3 away from  $\alpha$ -tubulin, opening the space needed for the neck-linker to dock against the motor core (Fig. 3e, f; left panels).

**Loop-2 modulates CaKip3's catalytic function according to tubulin protofilament shape.** The fact that microtubule-bound CaKip3 showed more extensive loop-2-tubulin interactions in the open APO- and ANP-states compared to the closed AAF-state suggests that the interaction of loop-2 with the microtubule lattice restricts rotation of the minus subdomain of the motor domain (Figs. 2 and 3). To investigate this hypothesis experimentally, we designed and expressed a mutant version of the CaKip3-MDN construct, whose long loop-2 was replaced with the short loop-2 sequence found in human kinesin-1, HsKIF5B (Supplementary Fig. 1b; CaKip3-MDN<sub>L2-HsKHC</sub>), which does not contact  $\alpha$ -

tubulin in any of the available microtubule-bound or tubulin-bound kinesin-1 structures<sup>22,50,51</sup>. In line with our hypothesis, the cryo-EM structure of this CaKip3 construct bound to microtubules has a docked neck-linker and closed nucleotide pocket in the ATP-like state (Fig. 4b; MT-CaKip3-MDN<sub>L2-HsKHC</sub>-ANP), unlike the CaKip3-MDN construct with a full loop-2 (Fig. 4c; MT-CaKip3-MDN-ANP). These data show that the kinesin-8-specific elongated loop-2 acts as a tubulin tether on the microtubule lattice pre-ATP hydrolysis, preventing the motor from closing, and that removing the CaKip3 loop-2 residues that interact with the microtubule lattice enable the motor domain to form the closed conformation in the ATP-bound state. The MT-CaKip3-MDN<sub>L2-HsKHC</sub>-ANP structure also suggests that loop-2 of kinesin-8 is directly involved in inducing tubulin curvature because the tubulin conformational changes in this structure are less extensive than in the MT-CaKip3-MDC-AAF structure (Fig. 4d, Supplementary Fig. 7d, f; compare blue arrows on  $\alpha$ -tubulin).

To learn how the loop-2-tubulin interactions and motor domain conformations observed for microtubule-bound CaKip3 relate to its motile activity, we assessed the microtubule-gliding velocity of the CaKip3-MDN and CaKip3-MDN<sub>L2-HsKHC</sub> motors. The gliding data shows that elimination of the CaKip3 loop-2 increased the microtubule-gliding speed of the motor by over threefold (Fig. 4e, g and Supplementary Fig. 8a). Conversely, when loop-2 of CaKip3 was grafted into an equivalent kinesin-1 construct (HsKHC-MDN<sub>L2-CaKip3</sub>), the microtubule-gliding speed slowed twofold (Fig. 4f, g and Supplementary Fig. 8a). One explanation for these results is that the interaction of loop-2 with straight  $\alpha\beta$ -tubulin protofilaments delays hydrolysis of ATP by the motor domain, thereby limiting the neck-linker docking event that enables forward stepping. An alternative, but not mutually exclusive explanation, is that the loop-2-tubulin interaction limits the stepping velocity of CaKip3 by increasing microtubule affinity. To distinguish between these two possibilities, we assessed the microtubule-stimulated ATPase activity of CaKip3-MDN, CaKip3-MDN<sub>L2-HsKHC</sub>, HsKHC-MDN, and HsKHC-MDN<sub>L2-CaKip3</sub> at steady state, and then measured the microtubule affinity of these proteins using a sedimentation assay. The data from the ATPase experiments show that CaKip3-MDN<sub>L2-HsKHC</sub> is ~1.6-fold faster at hydrolyzing ATP on microtubules than CaKip3-MDN (Fig. 4h, j). Likewise, the microtubule-stimulated ATP turnover by HsKHC-MDN<sub>L2-CaKip3</sub> was almost twofold slower than HsKHC-MDN (Fig. 4i, j). Our microtubule-binding



data showed that *CaKip3*-MDN has ~35-fold higher affinity for microtubules than *CaKip3*-MDN<sub>L2-HsKHC</sub> when AMP-PNP occupies the nucleotide-binding pocket (Fig. 4k, m and Supplementary Fig. 8b). The *HsKHC*-MDN<sub>L2-CaKip3</sub> construct also had a sevenfold greater affinity for the microtubule in the ATP-like state compared to *HsKHC*-MDN (Fig. 4l, m and Supplementary Fig. 8c). These results demonstrate that the extended loop-2 of *CaKip3* both increases the lifetime of the

microtubule-bound state and limits ATPase activity of the motor domain on the microtubule lattice.

To understand the functional effects of the loop-2-tubulin interactions observed in the curved tubulin-bound structure of *CaKip3*, we compared the dolastatin-stabilized tubulin-ring (D-ring)-stimulated ATPase activities of *CaKip3*-MDN and *CaKip3*-MDN<sub>L2-HsKHC</sub>. Our data shows that ATP hydrolysis by *CaKip3*-MDN<sub>L2-HsKHC</sub> was twofold slower than *CaKip3*-MDN on D-rings

**Fig. 2 Conformational changes in CaKip3 and tubulin.** **a** Displacement vectors for C $\alpha$  atoms in CaKip3 when comparing the microtubule-unbound CaKip3-MDN-ADP structure and the MT-CaKip3-MDC-APO complex. The models were aligned to microtubule interacting regions H4, loop-11 and loop-8 of the MT-CaKip3-MDC-APO structure, specifically, residues 249–257 and 350–379. Displacement vectors for C $\alpha$  atoms in CaKip3 and tubulin when comparing **b** MT-CaKip3-MDC-APO and MT-CaKip3-MDC-ANP, **c** MT-CaKip3-MDC-ANP and MT-CaKip3-MDC-AAF, and **d** MT-CaKip3-MDC-ANP and CT-CaKip3-MDC-ANP. All structures in **b–d** were aligned to the  $\beta$ -tubulin chain of the MT-CaKip3-MDC-APO complex. Displacement vectors for C $\alpha$  atoms are colored regionally to match the segment of the protein model that is compared, using the color scheme in Fig. 1. Views are from the minus end, down the long axis of the protofilament (left), side view (middle) and close-up of the tubulin interface (right). In each panel, the structure indicated on the left side of the arrow is shown as semi-transparent colored ribbons using the same regional color scheme as in Fig. 1. Only vectors with a magnitude of 1.0 Å or higher are shown.

(Fig. 5a, d). This reduction in ATPase activity without the full loop-2 region does not appear to be limited by D-ring binding ability because we observed a large proportion of the total CaKip3-MDN<sub>L2-HsKHC</sub> protein sedimented with D-rings using a co-sedimentation analysis (Supplementary Fig. 9a). Together with our structural data, these results show that the extended CaKip3 loop-2 functions like a tubulin protofilament shape sensor that modulates the motility and ATPase activity of the motor domain according to the shape of the tubulin protofilament it binds.

When we explored the tubulin shape-sensing ability of CaKip3's loop-2 further using unpolymerized free tubulin, which is also thought to be in the curved conformation<sup>52,53</sup>, we observed similar experimental results. CaKip3-MDN<sub>L2-HsKHC</sub> exhibited almost no free tubulin-stimulated activity, while CaKip3-MDN had a free tubulin-stimulated ATPase activity that is comparable to other kinesin-8s (Fig. 5b, e)<sup>1,32</sup>. Moreover, insertion of the CaKip3 loop-2 into HsKHC increased free tubulin-stimulated ATPase activity threefold (Fig. 5c, e); opposite its effect on microtubule-stimulated ATPase activity (Fig. 4i, j). These changes in tubulin-stimulated ATPase activity, brought about by swapping the loop-2 region, do not appear to be fully explained by a lack of tubulin binding because a large proportion of the total CaKip3-MDN<sub>L2-HsKHC</sub> protein eluted with DARPIn-capped  $\alpha\beta$ -tubulin during size-exclusion chromatography (SEC) analysis (Supplementary Fig. 9b; fractions 13.5–15 mL). However, loop-2-tubulin contacts observed in our CaKip3 structures do appear to be important tubulin-affinity determinants because insertion of CaKip3's loop-2 into kinesin-1 (HsKHC-MDC<sub>L2-CaKip3</sub>) increased the amount of motor that co-eluted with  $\alpha\beta$ -tubulin-DARPIn relative to HsKHC-MDC (compare Supplementary Fig. 9c, d; fractions 12–12.5 mL).

**Loop-1 and loop-2 are key drivers of microtubule-depolymerization.** In addition to the altered loop-2-tubulin interface and closed conformation of the motor domain of CaKip3 bound to curved tubulin (CT-CaKip3-MDC-ANP), a striking finding in this complex is the appearance of map density for loop-1 against the minus end neighboring CaKip3 motor domain (Fig. 1f). This head-to-tail interaction of CaKip3s is formed by the long polyasparagine repeat region of loop-1 (Supplementary Fig. 1a), which inserts into the deep groove between the loop-8 lobe and the core  $\beta$ -sheet of the minus end neighbor motor domain (Fig. 6a, b). When the CaKip3 nucleotide-binding pocket closes upon binding curved tubulin and the inlet and outlet strands of the loop-8 lobe move towards helix-12 of  $\beta$ -tubulin (Fig. 2d), this cavity opens, and loop-1 of the plus-end neighbor kinesin inserts and interacts with the minus end neighbor kinesin motor domain. Another remarkable feature is the formation of an  $\alpha$ -helix in the sequence that precedes the polyasparagine region (Fig. 6a, right panel). This helix is an extension of helix-0 and likely forms when the polyasparagine region is stabilized against the adjacent motor. These interactions demonstrate that loop-1 and loop-8 facilitate oligomerization of CaKip3 upon binding a curved tubulin protofilament. Weaker

loop-1 density is also present in the MT-CaKip3-MDC-AAF complex above the loop-8 lobe and likely represents a similar loop-1-mediated motor-motor interaction (Supplementary Fig. 10). No equivalent loop-1 density is observed in the MT-CaKip3-MDC-APO or -ANP structures. Taken together, these data suggest that loop-1 interactions with a minus end neighbor motor domain are stabilized by CaKip3 adopting a closed conformation, and that insertion of loop-1 into the other motor domain could potentially stabilize its closed conformation.

Using a sedimentation assay that separates microtubules from soluble tubulin subunits, we monitored GMP-CPP-stabilized microtubule depolymerization by CaKip3-MDN, a CaKip3-MDN construct lacking loop-1 (CaKip3-MDN <sub>$\Delta$ L1</sub>), the loop-2 swap construct (CaKip3-MDN<sub>L2-HsKHC</sub>), and a CaKip3-MDN<sub>L2-HsKHC</sub> construct lacking loop-1 (CaKip3-MDN<sub>L2-HsKHC+ $\Delta$ L1</sub>). Analysis of these reactions by SDS-PAGE revealed that loop-1 and loop-2 are both important for CaKip3's microtubule-depolymerase activity, and that loss of loop-2 causes the most impairment of this activity (Fig. 6c and Supplementary Fig. 11). CaKip3-MDN was 2.5-fold more active than CaKip3-MDN <sub>$\Delta$ L1</sub> and sevenfold more active than CaKip3-MDN<sub>L2-HsKHC</sub> at depolymerizing microtubules (Fig. 6c). Loss of loop-1 and loop-2 simultaneously (CaKip3-MDN<sub>L2-HsKHC+ $\Delta$ L1</sub>) resulted in a 19-fold decrease in microtubule depolymerization activity (EC<sub>50</sub>). These dramatic effects of loop-1 and loop-2 truncation support the functional importance of these regions in the microtubule depolymerization activity of CaKip3.

The small amount of microtubule depolymerization activity retained by CaKip3-MDN<sub>L2-HsKHC+ $\Delta$ L1</sub> shows that loop-1 and loop-2 are not the only features of the motor domain involved in catalyzing this process. The inability of HsKHC-MDN<sub>L2-CaKip3</sub> to depolymerize microtubules (Fig. 6d) and the tubulin curvature that we observe in the CaKip3-MDN<sub>L2-HsKHC</sub>-ANP complex (Fig. 4d) further support this idea. Overall, our structural data show that the closed nucleotide-binding pocket conformation of the motor domain actively induces tubulin curvature, which likely accounts for the residual depolymerization activity of the CaKip3-MDN<sub>L2-HsKHC+ $\Delta$ L1</sub> construct. Cataloging the differential tubulin contacts made by the open and closed conformations of the motor highlights that several closed-conformation-specific contacts are formed besides those in loop-2 (Supplementary Fig. 12). While many of these interactions likely contribute to the bending of tubulin, loop-2 adds to the tubulin-curving ability of the motor. This is supported by the greater degree of  $\alpha$ -tubulin displacement relative to  $\beta$ -tubulin between the MT-CaKip3-MDC-ANP and MT-CaKip3-MDC-AAF complexes than between the MT-CaKip3-MDN<sub>L2-HsKHC</sub>-APO and MT-CaKip3-MDN<sub>L2-HsKHC</sub>-ANP complexes (Supplementary Fig. 7d, f). Moreover, the loss of microtubule depolymerization activity caused by elimination of loop-1 (CaKip3-MDN <sub>$\Delta$ L1</sub>) indicates that loop-1's interactions with the minus end neighboring motor domain are also involved in the microtubule depolymerization mechanism of CaKip3. These interactions may allow the linked motor domains to act cooperatively (Fig. 1f and Supplementary Fig. 4b).



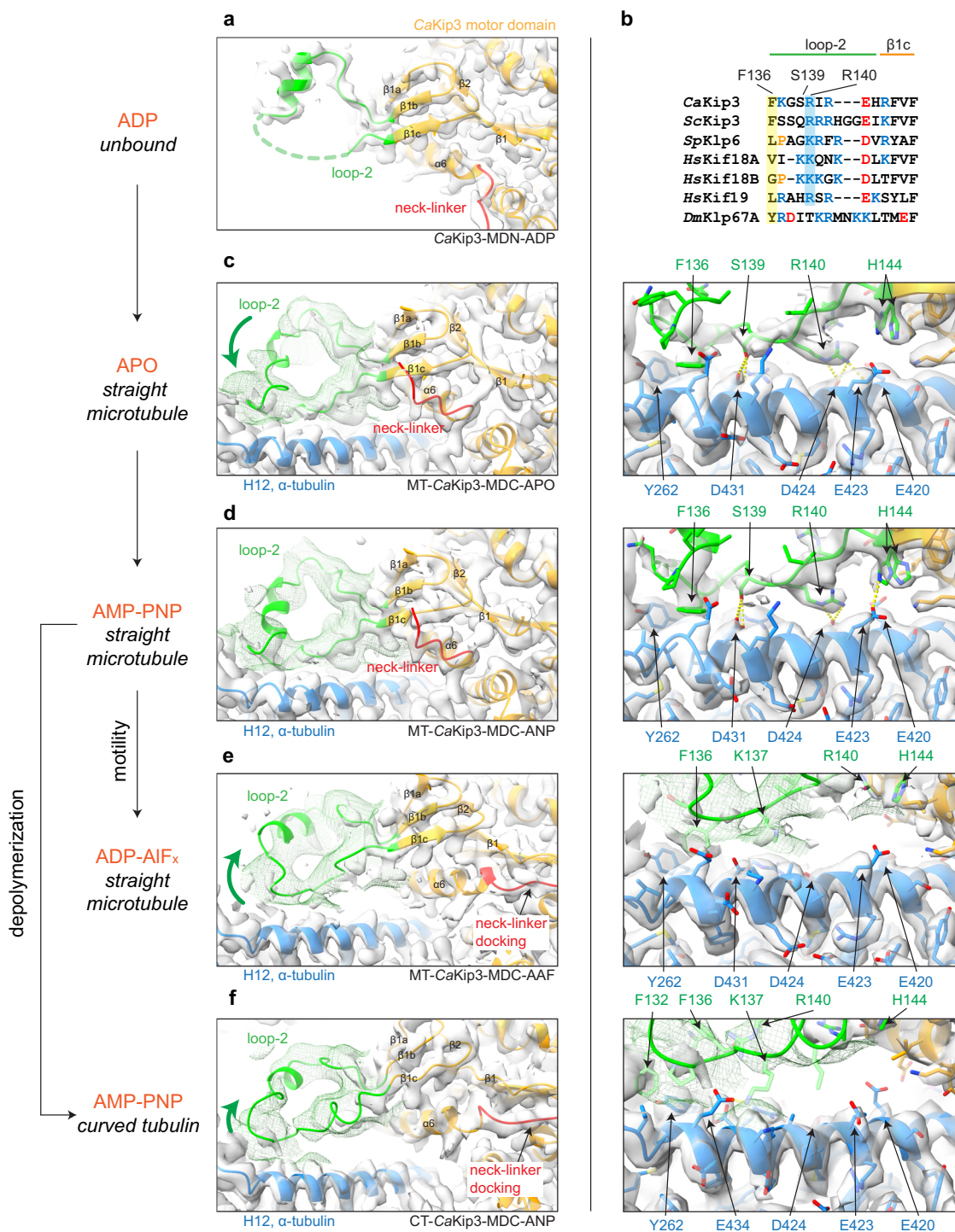
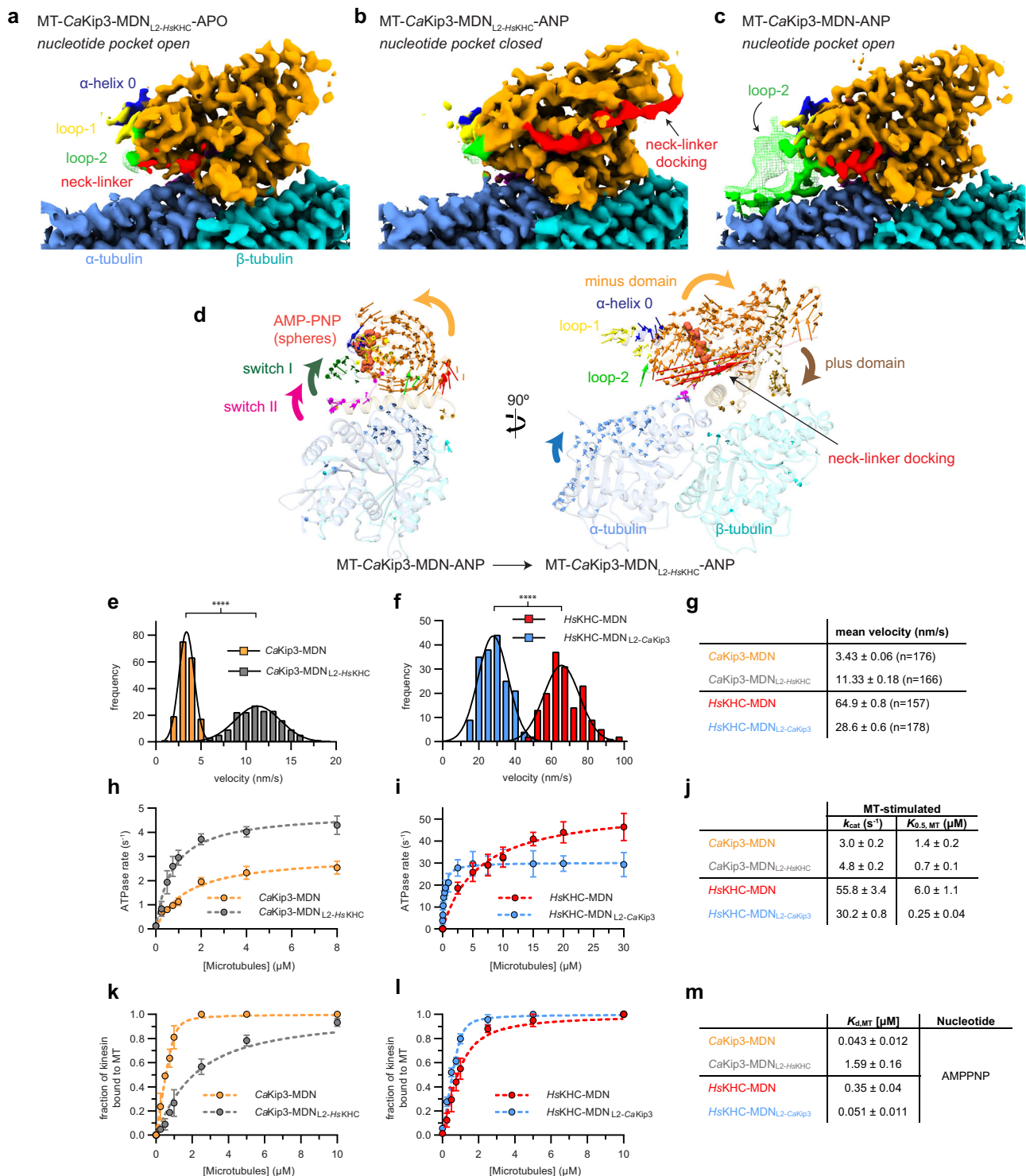


**Fig. 3** Loop-2 electron and cryo-EM densities and tubulin contacts. **a**  $2mF_{obs} - dF_{calc}$  electron density map (contoured at  $1.0 \sigma$ ) and cartoon model of loop-2 and the motor domain of the CaKip3-MDN crystal structure. **b** Sequence alignment of the tubulin contact region of CaKip3's loop-2 with other kinesin-8s. Conserved tubulin-binding residues are highlighted. Cryo-EM map and cartoon model of loop-2 of the **c** MT-CaKip3-MDC-APO complex, **d** MT-CaKip3-MDC-ANP complex, **e** MT-CaKip3-MDC-AAF complex, and **f** CT-CaKip3-MDC-ANP complex. Right panels show close-up view of loop-2-tubulin interactions for each complex. Green mesh maps were low-pass filtered at 7 Å (MT-CaKip3-MDC-AAF at 9 Å) to better display the noisier density of loop-2. Interacting residues are shown in stick representation. Pseudo-bonds between interacting atoms were determined and displayed using the “find clashes and contacts” routine in UCSF ChimeraX and are represented as yellow dashed lines.

**Discussion**

The central focus of this research was to understand the mechanistic basis for the dual ability of kinesin-8 motors to move processively on microtubules and to depolymerize microtubule plus-ends. To achieve this, we obtained cryo-EM structures that

demonstrate how the unique features of a kinesin-8 motor domain interact with  $\alpha\beta$ -tubulin subunits in the microtubule lattice and on microtubule ends. We also obtained functional data to show how the motor domain conformation and catalytic activity affects, and is affected by, the distinctive shapes of these



tubulin polymers. Our findings demonstrate that, when kinesin-8 encounters curved tubulin protofilaments, or protofilaments that can become curved, which are found at the microtubule plus-end, its motor domain readily forms a pro-depolymerization state (Fig. 7). In this state, the elongated loop-2 region moves toward the motor core to accommodate the position of  $\alpha$ -tubulin in curved  $\alpha\beta$ -tubulin subunits. This displacement of loop-2 is accompanied by closing of the ATP pocket to form a nucleotide-hydrolysis-competent active site and a docked neck-linker. In addition, loop-1 becomes more structurally ordered and inserts into the deep groove between loop-8 and the core  $\beta$ -sheet of the

preceding motor domain. By maintaining loop-2 contacts with tubulin, and the loop-1 linkage between motors, the conformational transition of multiple motor domains to a closed conformation could increase tubulin protofilament curvature enough to trigger microtubule depolymerization. Alternatively, when kinesin-8 binds tubulin protofilaments that are constrained to a straight conformation by the lateral protofilament interactions of the microtubule lattice, the interactions between loop-2 and  $\alpha$ -tubulin restrict the motor domain from transitioning to the closed conformation with a docked neck-linker. Unable to stably interact with the preceding motor via loop-1, or to curve tubulin enough

**Fig. 4 Structures and activity of loop-2 swap mutants on microtubules.** Cryo-EM map of **a** MT-CaKip3-MDN<sub>L2-HsKHC</sub> in the APO state, **b** MT-CaKip3-MDN<sub>L2-HsKHC</sub> in the AMP-PNP state, and **c** MT-CaKip3-MDN in the AMP-PNP state. **d** Displacement vectors for C $\alpha$  atoms in CaKip3 and tubulin when comparing the MT-CaKip3-MDN-ANP and MT-CaKip3-MDN<sub>L2-HsKHC</sub>-ANP complexes. Structures were aligned to the  $\beta$ -tubulin chain of MT-CaKip3-MDC-ANP. Displacement vectors for C $\alpha$  atoms are colored regionally to match the segment of the protein model that is compared, using the color scheme in Fig. 1. MT-CaKip3-MDN-ANP structure is shown as semi-transparent colored ribbons using the same regional color scheme as in Fig. 1. Only vectors with a magnitude of 1.0 Å or higher are shown. **e, f** Microtubule-gliding assay velocity distributions for CaKip3-MDN, CaKip3-MDN<sub>L2-HsKHC</sub>, HsKHC-MDN, and HsKHC-MDN<sub>L2-CaKip3</sub> using taxol-stabilized microtubules.  $n = 3$  independent experiments for each protein. Asterisks indicate two-tailed unpaired  $t$ -test significance:  $p = 1.3e-135$ ,  $p = 3.8e-122$  for **e** and **f**, respectively. **g** Summary of motor velocities. Values are presented as mean  $\pm$  SEM. **h** Microtubule-stimulated ATPase kinetics of CaKip3-MDN and CaKip3-MDN<sub>L2-HsKHC</sub> at steady state ( $n = 3$  independent experiments). The basal rate was  $0.13 \pm 0.01 \text{ s}^{-1}$  for both motors. Mean values ( $\pm$ SD) are shown. **i** Microtubule-stimulated ATPase kinetics of HsKHC-MDN and HsKHC-MDN<sub>L2-CaKip3</sub> at steady state ( $n = 3$  independent experiments). Basal rates were  $0.012 \pm 0.001 \text{ s}^{-1}$  and  $0.010 \pm 0.001 \text{ s}^{-1}$ , respectively. Mean values ( $\pm$ SD) are shown. **j** Summary of the microtubule-stimulated ATPase activities of the motors. Values are presented as mean  $\pm$  SEM. Data was fit to the Michaelis-Menten equation using GraphPad Prism to obtain  $K_{0.5, \text{MT}}$  and  $k_{\text{cat}}$  values. **k** Microtubule-co-sedimentation data for CaKip3-MDN and CaKip3-MDN<sub>L2-HsKHC</sub> ( $1 \mu\text{M}$  each) in the presence of 2 mM MgAMP-PNP ( $n = 3$  independent experiments). Mean values ( $\pm$ SD) are shown. **l** Microtubule-co-sedimentation data for HsKHC-MDN and HsKHC-MDN<sub>L2-CaKip3</sub> ( $1 \mu\text{M}$  each) in the presence of 2 mM MgAMP-PNP ( $n = 3$  independent experiments). Mean values ( $\pm$ SD) are shown. Taxol-stabilized microtubules were pelleted by centrifugation to separate the free kinesin and microtubule-bound kinesin. SDS-PAGE and Coomassie brilliant blue staining were used to determine the fraction of microtubule-bound kinesin. **m** Microtubule-binding affinities ( $K_{\text{D}}$  values) of the motors were calculated using the quadratic equation given in Materials and Methods. Values are presented as mean  $\pm$  SEM for three independent experiments. Source data are provided in the Source Data file.

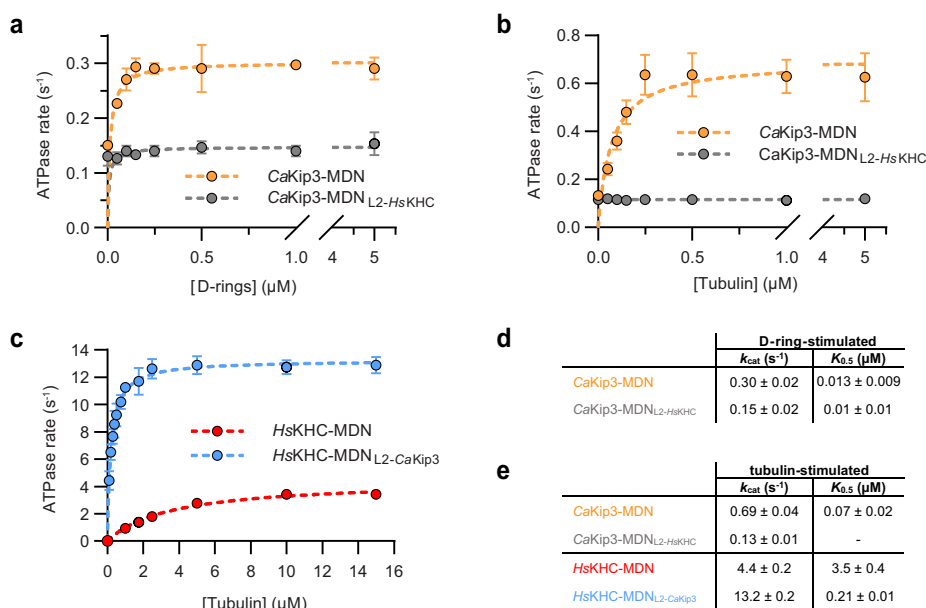


**Fig. 5 Activity of loop-2 swap mutants on curved tubulin.** **a** Dolastatin-induced tubulin-ring (D-ring)-stimulated ATPase kinetics of CaKip3-MDN and CaKip3-MDN<sub>L2-HsKHC</sub> at steady state ( $n = 3$  independent experiments). Mean values ( $\pm$ SD) are shown. **b** Free tubulin dimer-stimulated ATPase kinetics of CaKip3-MDN and CaKip3-MDN<sub>L2-HsKHC</sub> at steady state ( $n = 3$  independent experiments). Mean values ( $\pm$ SD) are shown. **c** Free tubulin dimer-stimulated ATPase kinetics of HsKHC-MDN and HsKHC-MDN<sub>L2-CaKip3</sub> at steady state ( $n = 3$  independent experiments). Mean values ( $\pm$ SD) are shown. **d** Summary of the D-ring-stimulated ATPase activities of the motors. Values are presented as mean  $\pm$  SEM. Data were fit to the Michaelis-Menten equation using GraphPad Prism to obtain  $K_{0.5, \text{MT}}$  and  $k_{\text{cat}}$  values. Source data are provided in the Source Data file.

to disrupt protofilament contacts, some of the loop-2-tubulin bonds eventually break, allowing the motor domain to form the pro-motility state, in which the neck-linker docks and the tethered head is moved to the next  $\alpha\beta$ -tubulin subunit.

Our structural results demonstrate that the closed conformation of the CaKip3 nucleotide-binding pocket not only accommodates the curved conformation of tubulin but also actively induces tubulin curvature (Figs. 2–4 and Supplementary Fig. 7). Comparing the microtubule structures with the CaKip3 motor domain in the open or closed conformations indicates that motor domain closure is accompanied by tubulin structural changes toward the curved conformation. This conformational change occurs with or without an intact loop-2 but appears more extensive in the former case. These results indicate that loop-2 is

important but not essential for kinesin-8 induced tubulin bending. This could explain the residual depolymerization activity we and others observe with kinesin-8 constructs with a mutated or deleted loop-2. (Fig. 6c)<sup>28,32</sup>. Previously, it was reported that loop-11 acts to recognize the curved conformation of tubulin by selectively interacting with an aspartate residue on  $\alpha$ -tubulin when tubulin is curved (Asp118—yeast tubulin, Asp116—bovine or porcine tubulin)<sup>28</sup>. This interaction was proposed to suppress the ATPase activity of the motor at the microtubule plus-end, leading to prolonged plus-end binding and subsequent microtubule depolymerization. In our CT-CaKip3-MDC-ANP structure, loop-11 residues are not within bonding distance of Asp116/118 and we observe no structural evidence of this interaction (Supplementary Fig. 13). While we cannot rule out the possibility

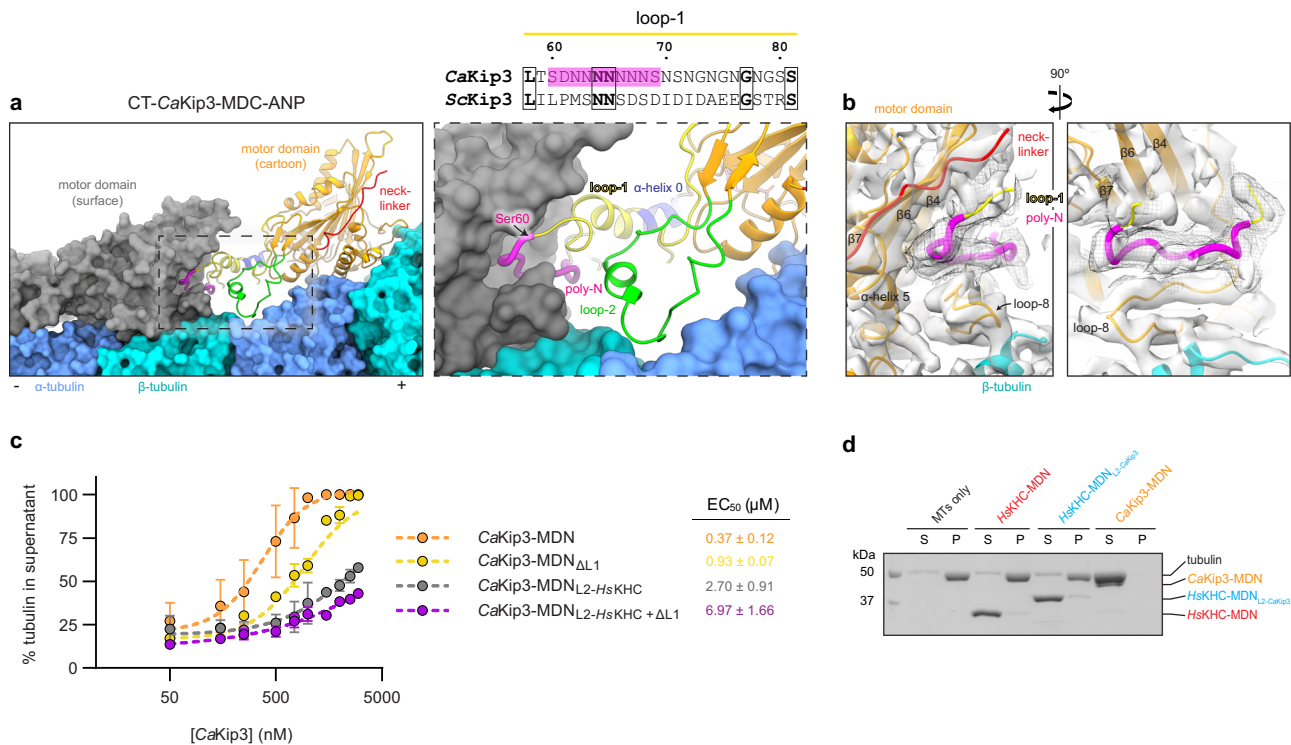


**Fig. 6 Loop-1 and loop-2 are major contributors to microtubule depolymerization activity.** **a** Cartoon representation of CaKip3 in the CT-CaKip3-MDC-ANP complex showing the polyasparagine section of loop-1 (magenta) inserted into the preceding motor domain (shown in surface representation). The insert shows “close up” view of the polyasparagine section in order to visualize structural elements involved in complex formation. Sequence alignment shows polyasparagine section of loop-1 in CaKip3 compared to ScKip3. **b** Cryo-EM map of the CT-CaKip3-MDC-ANP complex. A low-pass filtered map (5 Å) is shown as a black mesh around the polyasparagine track of loop-1. **c** Microtubule depolymerization by sedimentation dose-response curves for the indicated CaKip3 proteins. 2 μM GMP-CPP-stabilized microtubules were incubated with increasing concentrations of CaKip3-MDN, CaKip3-MDN<sub>ΔL1</sub>, CaKip3-MDN<sub>L2-HsKHC</sub>, or CaKip3-MDN<sub>L2-HsKHC+ΔL1</sub> in the presence of ATP. The data from three independent experiments were analyzed and fit to the four-parameter logistic equation. Mean values (±SD) are shown. EC<sub>50</sub> values are presented as the mean ± SEM. **d** Depolymerization of 2 μM GMP-CPP-stabilized microtubules by 3 μM of HsKHC-MDN, 3 μM HsKHC-MDN<sub>L2-CaKip3</sub>, and 1 μM CaKip3-MDN assessed by sedimentation. Reactions were incubated for 20 min in the presence of 20 mM MgATP, then free tubulin and microtubule polymers were separated into supernatant (S) and pellet (P) fractions by ultra-centrifugation. Equal portions of (S) and (P) were loaded and analyzed on a 10% Coomassie blue-stained SDS-PAGE gel. Similar results were obtained from two independent experiments. Source data are provided in the Source Data file.

that the conformation of loop-11 on curved tubulin may limit ATPase activity, our structures suggest Asp116/118 is not a major tubulin contact.

We observe that the mechanochemical cycle of a motile depolymerase is distinct from that of a strictly motile or strictly depolymerizing kinesin. During motility, the CaKip3 nucleotide-binding pocket remains in the open conformation following ATP binding. This is similar to the conformation of the depolymerizing kinesin-13s following ATP binding, and dissimilar from motile motors whose nucleotide pockets close in the equivalent nucleotide state. The fact that kinesin-8s and kinesin-13s both have elongated loop-2 regions that make microtubule contacts is further support of the hypothesis that loop-2 is also responsible for the open nucleotide-binding pocket of AMP-PNP-bound kinesin-13<sup>24</sup>. On the other hand, a pro-motility microtubule-bound state for kinesin-13s with a closed nucleotide-binding pocket and docked neck linker has not been reported. Differences between the loop-2 of kinesin-8s and kinesin-13s appear well suited for the different functionalities of these kinesins. The rigid kinesin-13 loop-2 inserts into the tubulin inter-dimer interface and makes similar contacts whether tubulin is in the straight or curved tubulin conformations<sup>24,27</sup>. However, to maintain these contacts the motor domain must be in the open conformation when interacting with straight tubulin and in the closed conformation when interacting with curved tubulin. In the case of

kinesin-8s a less structured loop-2 can form alternate contacts with tubulin allowing the motor domain to close and reach the pro-motility state while bound to straight tubulin in the microtubule lattice.

While the loop-2 region of kinesin-13s has a highly conserved motif (KVD) that is critical for microtubule depolymerization<sup>47,49,54</sup>, the loop-2 of kinesin-8s is not highly conserved. As we show here, and as others have previously reported, it is important but not essential for microtubule depolymerization (Fig. 6c, d)<sup>28,32</sup>. Our results also agree with previous experiments demonstrating that mutations to the kinesin-8 loop-2 can impart faster motility of monomeric constructs<sup>32</sup>, and that kinesin-1 grafted with enough kinesin-8 parts (loop-2, loop-11, and the neck) has depolymerization activity but is a slower motor<sup>28,32</sup>. We now build on these previous findings and clarify the role of loop-2 as a structural element that controls whether CaKip3 takes on a pro-motility or pro-depolymerization conformation, based on tubulin curvature.

Other studies of ScKip3 showed that kinesin-8 acts cooperatively to mediate length-dependent microtubule depolymerization<sup>2,4</sup>. Our structure of CaKip3 bound to D-rings provides a possible explanation for the cooperative mechanism of kinesin-8 microtubule depolymerization activity. We show that loop-1 (and loop-2) enable formation of linear arrays of motor domains on curved tubulin protofilaments. α-helix-0 extends toward the end of

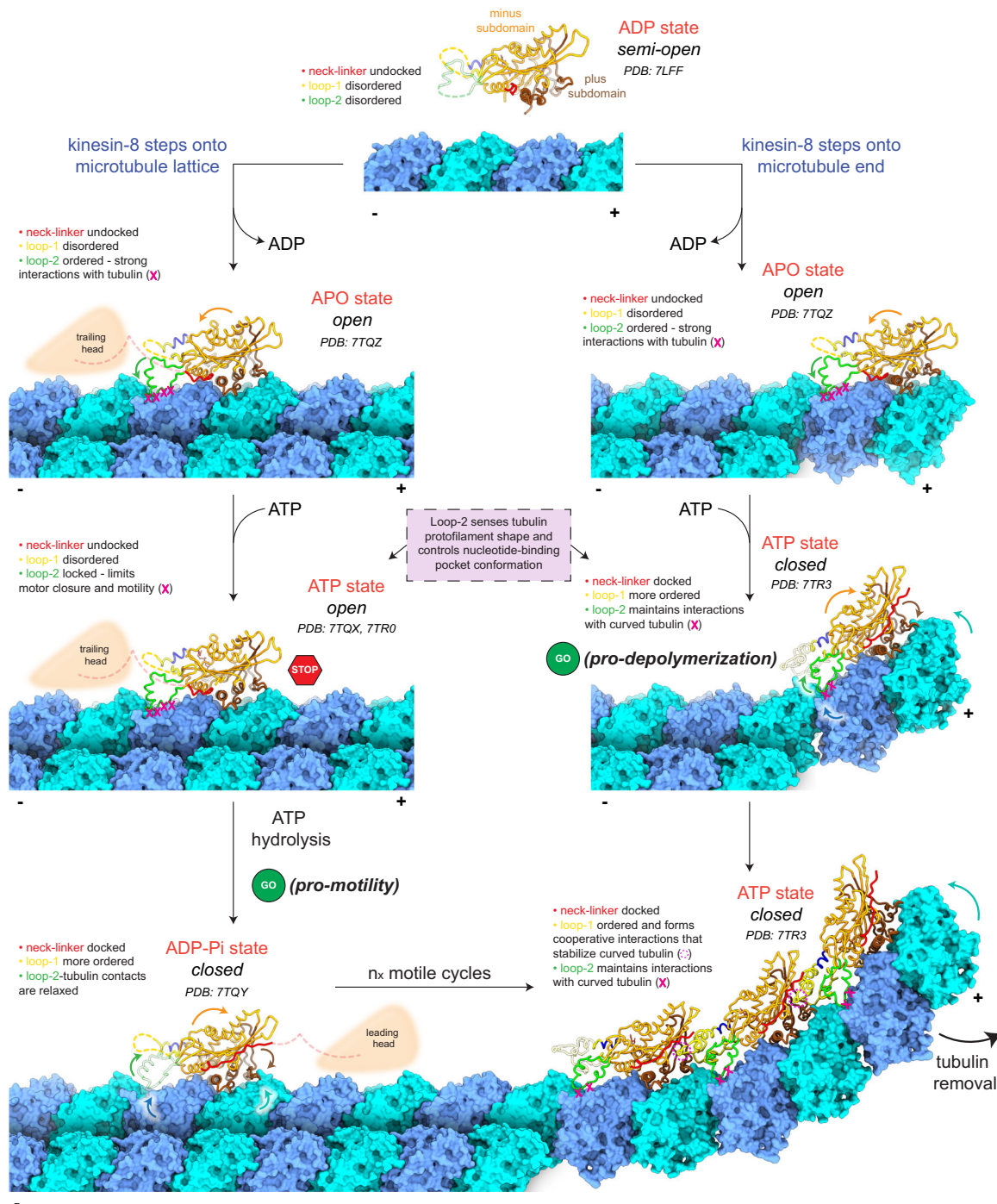


**Fig. 7 Model for tubulin shape-induced alternations between pro-motility and pro-depolymerization states of kinesin-8.** When kinesin-8 binds tubulin protofilaments that are constrained to a straight conformation by the lateral protofilament interactions of the microtubule lattice (left), the interactions between loop-2 and  $\alpha$ -tubulin restrict the motor domain from transitioning to the closed conformation with a docked neck-linker. Unable to stably interact with the preceding motor via loop-1, or to curve tubulin enough to disrupt protofilament contacts, some of the loop-2-tubulin bonds eventually break, allowing the motor domain to form the pro-motility state, in which the neck-linker docks and the tethered head is moved to the next  $\alpha\beta$ -tubulin subunit. Alternatively, when kinesin-8 encounters curved tubulin protofilaments, or protofilaments that can become curved, which are found at the microtubule plus-end (right), its motor domain readily forms a pro-depolymerization state. In this state, the elongated loop-2 region moves toward the motor core to accommodate the position of  $\alpha$ -tubulin in curved  $\alpha\beta$ -tubulin subunits. This displacement of loop-2 is accompanied by closing of the ATP pocket to form a nucleotide-hydrolysis-competent active site and a docked neck-linker. In addition, loop-1 becomes more structurally ordered and inserts into the deep groove between loop-8 and the core  $\beta$ -sheet of the preceding motor domain. By maintaining loop-2 contacts with tubulin, and the loop-1 linkage between motors, the conformational transition of multiple motor domains to a closed conformation could increase tubulin protofilament curvature enough to trigger microtubule depolymerization.

the docked neck-linker of the proximal motor domain and then transitions into a turn near Asp55 of loop-1 that inserts into the space between the loop-8 lobe and the core  $\beta$ -sheet. Three segments of loop-1 contact the adjacent motor domain, burying  $\sim 1075 \text{ \AA}^2$  of the adjacent motor domain surface. The polyasparagine track in loop-1 (including residues Asn62, Asn64, Asn65, Asn66, Ser69, Asn70, Ser71, Asn78, Gly79) forms the key part of this interaction, and some of this track is conserved in ScKip3. In ScKip3, two Asn residues are followed by a Ser/Asp and Ile/Asp repeat in the homologous region (Fig. 6a and Supplementary Fig. 1a). Previous studies reported that polyasparagine tracks in loop-8 of yeast kinesin-5, Cin8, may be involved in oligomerization due to the aggregation-inducing effect these sequences can have<sup>55</sup>. The binding site for the polyasparagine track of loop-1 is formed when the loop-8 lobe separates from the core  $\beta$ -sheet of the adjacent motor domain. Lys261, Arg269, Phe326, Phe392, and Arg435 are repositioned and accommodate loop-1. Interestingly, the loop-8 lobe also separates from the motor core in the MT-CaKip3-MDC-AAF structure, and weak density for loop-1 insertion is visible, indicating that cooperative kinesin-8-mediated tubulin bending can begin on microtubule protofilaments that have minimal curvature.

In summary, these studies provide an understanding of how kinesin-8s function as dual-activity motor proteins. Our findings implicate loop-2 as a tubulin protofilament shape sensor that regulates conformational changes in the kinesin-8 motor domain, which can either induce curvature of protofilaments at the microtubule end, leading to microtubule depolymerization, or enable forward displacement of the neck linker for processive motility if the motor domain is bound to protofilaments in the microtubule lattice. They also provide a structural basis for the cooperative depolymerization activity that has been reported for members of this kinesin family.

## Methods

**C. albicans strain construction.** A complete list of the *C. albicans* strains and primers used for cell biology experiments are presented in Supplementary Tables 1 and 2. All plasmids and DNA cassettes were transformed into *C. albicans* using the lithium acetate/PEG/heat shock method<sup>56</sup>. *C. albicans* cell growth, manipulation, and selection was performed based on an established protocol<sup>57</sup>. To generate CF239 (*kip3* +  $\Delta$ ), the *LEU2* gene in pSN40<sup>58</sup> was amplified by primers P122/P123 to generate a cassette with the selectable marker flanked by homology immediately upstream and downstream of the *Kip3* ORF, and was transformed into CF027, and the upstream integration junction checked by primers P13/P124. To knockout the second allele of *Kip3* (CF254 *kip3*  $\Delta/\Delta$ ), the *HIS1* marker in pSN52<sup>58</sup> was amplified by primers P122/123, transformed into CF239, and checked by primers P12/P124. The complement strain CF360 (*kip3*  $\Delta/\Delta$  + *KIP3*<sup>+</sup>) was generated by first cloning the *KIP3* ORF +/– 1000 bp into a pCIP10-based integration vector<sup>59</sup> using primer pair P130/P131. Then, pCIP10 harboring *KIP3* was linearized with MluI, transformed into CF254 to create CF360, and checked for integration into one of the two endogenous *KIP3* loci using primer pairs P12/P16 and P13/P16.

Microtubules were fluorescently labeled in strains CF370, CF363, CF376, CF379, CF171, CF217, and CF230 using the pGAL1-Tub2-mCherry-Arg4::NEUT5L and pGAL1-Tub2-GFP-Sat1::NEUT5L plasmids as previously described<sup>57,59</sup>. pGAL1 plasmids were linearized with KpnI for integration at the NEUT5L locus, transformed into the indicated *C. albicans* strain (Supplementary Table 1), and checked using primer pairs P16/P107 and P17/P107.

SPC98 was labeled with GFP by amplifying pGFP-SAT1<sup>57</sup> with P108 and P109, transforming the cassette into CF370 (to generate CF363) or CF376 (to generate CF379), then confirming integration using primer pair P18/P110.

**C. albicans growth assays.** Assessment of *C. albicans* generation time was performed based on an established protocol<sup>57</sup>. Cells were diluted to  $2.5 \times 10^6$  cells/mL then grown in SDC medium at 30 °C. The number of cells/mL was counted every hour with a hemocytometer. Temperature-sensitivity spot assays were performed by diluting cells as indicated, then plating 5  $\mu$ L drops on YPD media and incubating plates for 48 h at the indicated temperature. Hyphal growth assays were performed by diluting cells to  $10^3$  cells/mL in phosphate-buffered saline, then plating 25  $\mu$ L on Spider medium. Plates were incubated for 5 days at 30 °C and then photographed.

**Microscopy of C. albicans cells.** Static images of live *C. albicans* cells were collected using a Zeiss Axio Observer Z1 fluorescence microscope with a 100x (1.40 NA) oil objective AxioCam hRM camera equipped with Axiovision software. Overnight cultures of cells grown in synthetic dropout (SD) media were immobilized between an SD agarose pad and a glass coverslip as previously described<sup>57</sup>. Chambers were sealed using a 1:1:1 mixture of petrolatum [Vaseline], lanolin, and paraffin. Images were captured in five z-stacks spaced 0.8  $\mu$ m apart, and maximum-intensity projection of z-stacks was conducted using ImageJ (version 1.53). Quantification of astral microtubule lengths was performed in ImageJ. Cell images were false colored in ImageJ and contrast was adjusted in Adobe Photoshop and Adobe Illustrator. Source data are provided in the Source Data file.

**Cloning.** The genes for *Candida albicans* *Kip3* and *Homo sapiens* kinesin heavy chain (*HsKHC/Kif5B*) were codon-optimized for expression in *E. coli* and ordered as chemically synthesized DNA fragments from Integrated DNA Technologies (IDT). For all kinesin constructs used in these studies (Supplementary Fig. 1a), gene fragments of the desired length were PCR amplified and cloned into pET-24d(+) using NcoI and XhoI, yielding a C-terminal 6X-His tag. Mutant genes were generated either through overlap-extension PCR (CaKip3-MDN<sub>L2-HsKHC</sub>, CaKip3-MDN <sub>$\Delta$ L1</sub>, CaKip3-MDN<sub>L2-HsKHC+ $\Delta$ L1</sub>) or ordered as chemically synthesized DNA (*HsKHC-MDC<sub>L2-CaKip3</sub>*). The CaKip3-MDN<sub>L2-HsKHC</sub> and CaKip3-MDN<sub>L2-HsKHC+ $\Delta$ L1</sub> constructs have the *HsKIF5B* loop-2 sequence “IASK” (residues I41-K44) replacing CaKip3 residues F116-H144. The CaKip3-MDN <sub>$\Delta$ L1</sub> and CaKip3-MDN<sub>L2-HsKHC+ $\Delta$ L1</sub> constructs have residues V44-G101 removed. The *HsKHC-MDN<sub>L2-CaKip3</sub>* and *HsKHC-MDC<sub>L2-CaKip3</sub>* constructs have the CaKip3 loop-2 sequence from F116-H144 replacing the *HsKIF5B* loop-2 sequence “IASK” (residues I41-K44). Constructs *HsKHC-MDC* and *HsKHC-MDC<sub>L2-CaKip3</sub>* contained a cleavable C-terminal TEV-SNAP-6X-His tag (SNAP-tag from NEB). DARPin-D2 was ordered as a codon-optimized gene product from IDT and cloned into pET16b using Gibson Assembly, producing an N-terminal 6X-His tag. All plasmids were sequenced to verify correct assembly.

**Expression and purification of recombinant proteins.** For all kinesin proteins and DARPin D2, the same general purification scheme was used. Plasmids encoding kinesins were transformed into *E. coli* BL21(DE3) cells (Agilent, 200131) and plasmids encoding DARPin D2 were transformed into BL21 RIL cells (Agilent, 230245). All proteins were expressed in Luria-Bertani (LB) media supplemented with the appropriate antibiotic. Protein production was induced with 1 mM isopropyl  $\beta$ -D-1-thiogalactopyranoside (IPTG) and cells were grown overnight between 16 and 25 °C. Cell pellets were lysed in lysis buffer (10 mM sodium phosphate, 300 mM NaCl, 2 mM MgCl<sub>2</sub>, 1 mM EGTA, 0.2 mM ATP, 5 mM 2-Mercaptoethanol (2-ME), 0.2 mg/mL lysozyme (Bioshop), Pierce Protease Inhibitor Tablets (Thermo), pH 7.2) using sonication. Clarified supernatant was loaded onto Ni-NTA resin (Qiagen) equilibrated in wash buffer (10 mM sodium phosphate, 300 mM NaCl, 2 mM MgCl<sub>2</sub>, 0.1 mM EGTA, 20 mM imidazole, 0.2 mM ATP, 5 mM 2-ME, pH 7.2) and resin was thoroughly washed with wash buffer. Target protein was eluted with elution buffer (wash buffer + 300 mM imidazole) then dialyzed overnight into HEPES buffer (20 mM HEPES, 1 mM MgCl<sub>2</sub>, 150 mM NaCl, 0.2 mM ATP, 1 mM dithiothreitol (DTT), pH 7.2). The next morning, samples were run over a Superdex 200 26/60 size-exclusion column (GE Healthcare) equilibrated with HEPES buffer. Fractions containing target protein were pooled, concentrated, flash frozen in liquid N<sub>2</sub>, and stored at –80 °C.

Tubulin was purified from bovine brains by two cycles of polymerization-depolymerization in a high-molarity PIPES buffer as described by Castoldi et al.<sup>60</sup>. Aliquots were flash frozen in liquid N<sub>2</sub> and stored at –80 °C until use.

## Preparation of taxol-stabilized microtubules and D-rings for biochemical assays

Taxol-stabilized microtubules were assembled as previously described with some modifications<sup>61</sup>. Soluble tubulin was diluted to 5 mg/mL in BRB80 buffer (80 mM PIPES, 1 mM MgCl<sub>2</sub>, 1 mM K-EGTA, 1 mM DTT, pH 6.8) supplemented with 2 mM GTP and depolymerized on ice for 10 min. The mixture was clarified by centrifugation at  $312,984 \times g$  (TLA-100; Beckman Coulter) for 5 min at 4 °C, then microtubule-polymerization was induced by addition of 10% DMSO and incubation at 37 °C. After 40 min, 20  $\mu$ M taxol (paclitaxel-d5, Toronto Research Chemicals) was added to the reaction mixture and incubation was continued at 37 °C for another 40 min. Microtubules were sedimented at  $312,984 \times g$  (TLA-100; Beckman Coulter) for 15 min at 25 °C and resuspended in the appropriate reaction buffer supplemented with 20  $\mu$ M taxol. Unless otherwise specified, microtubule concentration was determined by measuring optical density at 280 nm ( $A_{280}$ ). To avoid the light scattering effect of microtubule polymers, microtubules were depolymerized by incubation on ice and addition of 5 mM CaCl<sub>2</sub> prior to measuring  $A_{280}$ .

Dolastatin-induced tubulin rings (D-rings) were polymerized by diluting tubulin to 40  $\mu$ M in BRB80 buffer containing 80  $\mu$ M dolastatin-10 (APEXIO) and incubating the reaction for 1 h at 25 °C. Whenever D-rings were used in experiments, the concentration of dolastatin present was at least twofold more than the concentration of tubulin and never below a concentration of 20  $\mu$ M. Assembled D-rings were used within 2 h.

**ATPase assay.** ATP turnover by kinesins was measured when stimulated by taxol-stabilized microtubules, D-rings, or soluble tubulin. To prepare tubulin for the ATPase assays, tubulin stock was diluted to 1.7 mg/mL in A25 buffer (25 mM ACES, 2 mM MgAcetate, 2 mM K-EGTA, 0.1 mM K-EDTA, 1 mM 2-ME, pH 6.9), incubated on ice for 10 min, and clarified at  $312,984 \times g$  (TLA-100; Beckman Coulter) for 5 min at 4 °C. ATP turnover was measured using an enzyme-coupled system<sup>62,63</sup> and in specific cases the EnzChek Phosphate assay (Thermo Fisher) was also used to verify results (for tubulin and D-ring-stimulated CaKip3-MDN and CaKip3-MDN<sub>L2-HSKHC</sub>). For the enzyme-coupled system, reactions were prepared in A25 buffer containing 1 mM MgATP, 2 mM phosphoenol-pyruvate (K-PEP), 0.25 mM NADH, 60 µg/mL lactate dehydrogenase, 60 µg/mL pyruvate kinase, 20 µM taxol (for microtubule reactions), 20 µM dolastatin (for D-ring reactions), microtubules or D-rings or tubulin, and 200 nM kinesin (for kinesin-8 reactions) or 15 nM kinesin (for kinesin-1 reactions). Reactions containing soluble tubulin also included 0.5 mM GDP to hinder microtubule-polymerization. For the EnzChek Phosphate assay, reactions were prepared in A25 buffer and contained 2 mM MgATP, 200 µM 2-amino-6-mercapto-7-methylpurine riboside (MESG), 1 unit/mL purine nucleoside phosphorylase (PNP), 20 µM dolastatin (for D-ring reactions), D-rings or tubulin, and 200 nM kinesin-8. Using a SpectraMax iD3 plate reader (Molecular Devices),  $A_{340}$  values (enzyme-coupled system) or  $A_{360}$  values (EnzChek phosphate assay) were collected in 15-s intervals for 15 min. Rates of ATP turnover were determined from the initial linear portion of the data and fit to the Michaelis-Menten equation using GraphPad Prism 8.0 (GraphPad Software, San Diego, CA) to determine  $K_{0.5}$  and  $k_{cat}$ .

**Microtubule co-sedimentation assay.** Microtubule-kinesin co-sedimentation reactions were prepared and analyzed based on an established protocol<sup>62</sup> with the following modifications. Prior to setting up co-sedimentation reactions, kinesin motor was pre-cleared by centrifugation at  $312,984 \times g$  (TLA-100; Beckman Coulter) for 5 min at 4 °C. Co-sedimentation reactions were prepared in 100 µL volumes of BRB80 buffer supplemented with 100 mM KCl and contained 2 mM adenylyl-imidodiphosphate (AMP-PNP), 1 µM kinesin, 20 µM taxol, and 0–10 µM microtubules. Reaction mixtures were incubated for 20 min at 25 °C then centrifuged at  $139,104 \times g$  (TLA-100; Beckman Coulter) for 15 min at 25 °C. The 50 µL of the supernatants were retained, and the remainder was discarded. Pellets were resuspended in 100 µL BRB80 buffer and 50 µL was retained for SDS-PAGE analysis. Supernatant and pellet samples (10 µL per lane) were loaded on 10% SDS-PAGE gel, ran, and then were visualized by staining with Coomassie brilliant blue R-250. Band intensities were quantified with ImageJ and the percentage of kinesin complexed with the microtubule was plotted as a function of microtubule concentration. To obtain values for  $K_d$ , data was fit to a quadratic equation using GraphPad Prism 8.0:  $(MT \cdot E)/E = 0.5(E_0 + K_{d,MT} + MT_0) - [(E_0 + K_{d,MT} + MT_0)^2 - (4E_0MT_0)^{1/2}]$ , where  $E_0$  is the total kinesin concentration,  $MT \cdot E$  is the amount of kinesin bound to the microtubules,  $MT_0$  is the total microtubule concentration, and  $K_d$  is the dissociation constant.

**D-ring co-sedimentation assay.** D-ring co-sedimentation assays were performed based on an established protocol<sup>64</sup> with the following modifications. Kinesin motor was pre-cleared by centrifugation at  $312,984 \times g$  (TLA-100; Beckman Coulter) for 5 min at 4 °C. Co-sedimentation reactions were prepared in 100 µL volumes of BRB80 buffer containing 4 µM D-rings, 20 µM Dolastatin, 4 µM kinesin, and 2 mM AMP-PNP. Dolastatin was also present in control reactions that did not contain D-rings. Reactions were incubated for 10 min at 25 °C, then centrifuged at  $386,400 \times g$  (TLA-100; Beckman Coulter) at 25 °C for 15 min. The top 50 µL of the reaction supernatants were retained and the remainder was discarded. Pellets were resuspended in 100 µL BRB80 buffer and 50 µL was retained for SDS-PAGE analysis. Supernatant and pellet samples were analyzed on SDS-PAGE gels stained with Coomassie brilliant blue R-250.

**Motility assay.** Rhodamine-labeled taxol-stabilized microtubules were assembled based on an established protocol with the following changes<sup>65</sup>. Rhodamine-labeled porcine tubulin (Cytoskeleton Inc.) and unlabeled tubulin were mixed in a 1:7 molar ratio (5 mg/mL total tubulin) in BRB80 buffer supplemented with 10% DMSO and 2 mM GTP. The mixture was depolymerized on ice for 10 min, then clarified at  $312,984 \times g$  (TLA-100; Beckman Coulter) for 5 min at 4 °C. The supernatant was polymerized at 37 °C for 30 min, then diluted twofold with BRB80 buffer containing 40 µM taxol. The incubation was continued for another 30 min at 37 °C, then microtubules were sedimented at  $139,104 \times g$  at 25 °C for 15 min. The microtubules contained in the pellet were carefully resuspended in BRB80 buffer containing 40 µM taxol.

Flow chambers for the motility assay were constructed by adhering siliconized coverslips (Hampton Research) to microscopy slides using double-sided tape. The total chamber volume was roughly 8 µL. Three oxygen-scavenging mixtures (OSM) were prepared fresh for each experiment: OSM-0 (BRB80, 1.5 mM MgAc, 2 mM 2-ME, 200 µg/mL glucose oxidase, 175 µg/mL catalase, 25 mM glucose), OSM-1 (OSM-0 with addition of 1.5 mM AMP-PNP, 40 µM taxol), and OSM-2 (OSM-0 with 1.5 mM MgATP, 40 µM taxol). Stock anti-His antibody (Thermo Fisher, 05-949-MI) was diluted to 70 µg/mL in BRB80 buffer, flowed through the chamber, and allowed to adhere for 5 min. Chambers were washed with BRB80 buffer, then 1% F-127 pluronic acid in BRB80 buffer was added to block non-specific binding of

microtubules. After a 10-min incubation, chambers were washed with BRB80 buffer and 0.5 µM His-tagged kinesin diluted in OSM-0 was introduced into the chamber. Kinesin was allowed to bind to anti-His antibodies for 10 min, then a 1:60 dilution of rhodamine-labeled microtubules in OSM-1 was flowed into the chamber. After a 5-min incubation, OSM-2 was flowed into the chamber to remove unbound microtubules and initiate the reaction. Imaging was performed at 25 °C on an Olympus IX83 inverted fluorescence microscope equipped with an Andor Zyla 4.2 Plus camera controlled by Olympus cellSens software (version 1.17). Images were collected every 20 s for kinesin-8 timelapses and every 5 s for kinesin-1 timelapses. Microtubule velocity was calculated using ImageJ (NIH) by tracking the position of the microtubule end in each frame. The average distance traveled between each frame was divided by the time increment between frames to yield a velocity value for each microtubule. Histograms fit with Gaussian curves were generated in GraphPad Prism 8.0.

**Microtubule-depolymerization assay.** Assessment of microtubule-depolymerization by sedimentation was carried out as described with minor changes<sup>32</sup>. To assemble microtubules stabilized with guanylyl-( $\alpha$ ,(3)-methylene-diphosphonate (GMP-CPP) (Jena Bioscience), tubulin was diluted to 2 mg/mL in BRB80 buffer supplemented with 0.5 mM GMP-CPP. The mixture was incubated on ice for 10 min then clarified at  $312,984 \times g$  (TLA-100; Beckman Coulter), 5 min, 4 °C. The supernatant was polymerized at 37 °C for 1 h, then microtubules were sedimented at  $139,104 \times g$  (TLA-100; Beckman Coulter) for 15 min at 25 °C. Resuspended microtubules were then depolymerized, clarified, and re-polymerized to increase the occupancy of GMP-CPP within the microtubule lattice. The second microtubule-polymerization step was performed with 1 mM GMP-CPP. The final GMP-CPP-stabilized microtubules were sedimented at  $139,104 \times g$  (TLA-100; Beckman Coulter) for 15 min at 25 °C and resuspended in BRB80 buffer.

Sedimentation reactions were prepared as 50 µL of BRB80 buffer containing 2 µM GMP-CPP-stabilized microtubules, 20 mM MgATP and 0–3 µM kinesin. Reactions were incubated for 20 min at 25 °C then centrifuged at  $139,104 \times g$  (TLA-100; Beckman Coulter) for 15 min, 25 °C. The top 30 µL of the reaction supernatant was retained and the remainder was discarded. Pellets were resuspended in 50 µL BRB80 buffer and 30 µL was retained for SDS-PAGE analysis. Supernatant and pellet fractions were visualized by SDS-PAGE stained with Coomassie brilliant blue R-250. The intensity of tubulin in each fraction was quantified with ImageJ (NIH). The percentage of tubulin in the supernatant fraction was plotted as a function of kinesin concentration and values were fit to a four-parameter logistic equation using GraphPad Prism 8.0 to determine relative  $EC_{50}$  values.

**Analytical size-exclusion chromatography.** Analytical SEC experiments were performed based on an established protocol<sup>27</sup> with minor changes. A 200 µL reaction was prepared in HEPES buffer (20 mM HEPES, 1 mM MgCl<sub>2</sub>, 150 mM NaCl, 1 mM DTT, pH 7.2) containing 23 µM kinesin, 23 µM tubulin, 23 µM DARPin-D2, 0.1 mM GDP, and 0.2 mM AMPNP. Reactions were incubated on ice for 30 min, clarified at  $13,148 \times g$  for 10 min at 4 °C, then 100 µL of the mixture was loaded onto a Superdex 200 10/300 GL size-exclusion column (GE Healthcare) equilibrated in HEPES buffer. Fractions of interest (0.5 mL each) were concentrated using an Amicon Ultra filter with a 10 kDa cutoff for 10 min at  $13,148 \times g$ , 4 °C and the resulting volume was made up to 60 µL. Fractions were visualized by SDS-PAGE stained with Coomassie brilliant blue R-250. For specific samples, immunoblotting using HRP-conjugated anti-His antibody (Abcam, ab1187) was performed based on an established protocol<sup>66</sup>. Following SDS-PAGE of fractions diluted 1:20, a wet electroblot at 400 mA for 2 h was used to transfer proteins to a PVDF membrane. Membranes were blocked with 5% milk powder in TBST buffer (50 mM Tris, 150 mM NaCl, 0.05% Tween 20, pH 7.5) for 1 h. Membranes were incubated in anti-His antibody (diluted 1:1000 in blocking buffer) for 1 h. Membranes were washed three times with TBST at room temperature then incubated with the Pierce Enhanced Chemiluminescence Western Blotting Substrate (Thermo Fisher) prior to imaging. Blots were imaged using an Azure C300 Digital Imager.

**Crystallization of CaKip3-MDN-ADP.** Crystals of CaKip3-MDN-ADP were grown using hanging drop vapor diffusion by mixing the protein in a 1:1 ratio with a precipitant solution of 0.1 M MMT (Malic acid, MES and TRIS), 25% PEG 1500, pH 8 at 277 K. The total drop volume was 4 µL. Prior to mixing, the solution of purified kinesin protein (roughly 22 mg/mL) was supplemented with 1 mM ATP. Crystals took approximately 1 week to grow full-sized. Before collecting diffraction data, crystals were transferred to a cryoprotectant solution composed of 0.1 M MMT, 25% PEG 1500, 20% ethylene glycol, pH 8, and were flash frozen in liquid N<sub>2</sub>.

X-ray diffraction data for the CaKip3-MDN-ADP crystals were collected using the synchrotron beamline CMCF 08ID-1 of the Canadian Light Source (Saskatoon, Canada) at 100 K. The in-house software program AutoProcess developed at the CMCF was used to run XDS<sup>67</sup>, which processed and scaled the diffraction data and produced the reflection output file for structure determination. The initial CaKip3-MDN-ADP structure was solved by molecular replacement using the KIF18A motor domain (PDB: 3LRE) as a search model in MOLREP<sup>68</sup>. The final model was produced after several cycles of manual building in COOT<sup>69</sup> and structure

refinement using PHENIX<sup>70</sup>. Diffraction data collection and refinement statistics are summarized in Table 1.

**Cryo-EM samples preparation.** The datasets were collected on gold grids (UltrAuFoil R2/2 200 mesh) plasma cleaned just before use (Gatan Solarus plasma cleaner, at 15 W for 6 s in a 75% argon/25% oxygen atmosphere).

Fifteen-protofilament-enriched microtubules were prepared from porcine brain tubulin (Cytoskeleton, Inc. CO)<sup>24</sup>. Microtubules were polymerized fresh the day of the cryo-EM sample preparation. Kinesin aliquots were thawed on ice just before use. All nucleotides stock solutions used were prepared with an equimolar equivalent of MgCl<sub>2</sub> to ADP or AMP-PNP. Four microliters of a microtubule solution at 2–5 μM tubulin in BRB80 buffer supplemented with 20 μM paclitaxel were layered onto the EM grid and incubated for 1 min at room temperature. This microtubule solution also contained AMP-PNP at 4 mM or ADP at 4 mM plus 2 mM AlCl<sub>3</sub> and 10 mM KF for the AMP-PNP and ADP-AIF<sub>x</sub> conditions respectively. During the incubation time, a fraction of the thawed kinesin aliquot was diluted to prepare a 20-μM kinesin solution containing 20 μM paclitaxel and either of the three nucleotide conditions to be probed: (1) 4 mM AMP-PNP, (2) 4 mM ADP plus 2 mM AlCl<sub>3</sub>, and 10 mM KF (ADP-AIF<sub>x</sub> conditions) or (3) apyrase: 5 × 10<sup>-3</sup> units per μL (APO conditions). Then the excess microtubule solution was blotted from the grid using a Whatman #1 paper. Four microliters of the kinesin solution were then applied onto the EM grid, transferred to the chamber of a Vitrobot apparatus (FEI-ThermoFisher MA) at 100% humidity where it was incubated for 1 min at room temperature, and blotted for 2.5–3 s with a Whatman #1 paper and –2-mm offset before plunge-freezing into liquid ethane. Grids were clipped and stored in liquid nitrogen until imaging in a cryo-electron microscope.

Dolastatin-10 rings (D-rings) were made by incubating 80 μM porcine brain tubulin (Cytoskeleton, Inc. CO) with 160 μM dolastatin-10 (APEX BIO) in BRB80 buffer pH 6.8 and incubating for 1 h at 25 °C. That solution was then diluted to make the cryo-EM sample: 3 μM tubulin D-rings, 20 μM dolastatin-10, 12 μM CaKip3-MDC, 4 mM AMP-PNP in BRB80 buffer, pH 6.8.

**Cryo-EM data collection.** Data were collected at 300 kV on Titan Krios microscopes (Supplementary Table 3) equipped with K2 summit detectors for the microtubule datasets and with K3 detector for the CT-CaKip3-MDC-ANP dataset. Acquisition was controlled using Legion<sup>71</sup> with the image-shift protocol and partial correction for coma induced by beam tilt<sup>72</sup>. The defocus ranges and cumulated dose for all datasets are given in Table 2.

For the decorated microtubule samples, data collection was performed semi-automatically using one stage shift per hole and 4–6 exposures using image-shift per 2-μm diameter holes. The exposures were fractionated on 40–50 movie frames.

For the CT-CaKip3-MDC-ANP sample, data collection was performed semi-automatically targeting 5 holes per stage shift and 2 exposures using image-shift per 2-μm diameter holes. The stage was tilted 40 degrees to compensate for preferential orientation of the particles<sup>73</sup> (Supplementary Fig. 4). The other dataset used to make 2D class averages of the structures was collected similarly but with no stage tilt, targeting 5–6 holes per stage shift with 3 exposures per 2-μm diameter holes. The exposures were fractionated on 50 movie frames.

**Processing of the cryo-EM datasets of microtubule-kinesin complexes.** The processing was done as previously described<sup>21</sup>. Movie frames were aligned with motioncor2<sup>74</sup> generating both dose-weighted and non-dose-weighted sums and correcting for magnification anisotropy (Supplementary Table 3). Before each of the corresponding cryo-EM session, a series of ~20 micrographs on a cross-grating calibration grid with gold crystals was used to estimate the current magnification anisotropy of the microscope using the program mag\_distortion\_estimate v1.0<sup>75</sup>. Magnification anisotropy correction was performed within motioncor2 using the obtained distortion estimates (Supplementary Table 3). Contrast transfer function (CTF) parameters per micrographs were estimated with Gctf<sup>76</sup> on aligned and non-dose-weighted movie averages.

Helical reconstruction on 15R microtubules was performed using a helical-single-particle 3D analysis workflow in FREALIGN<sup>77</sup>, as described previously<sup>21,24</sup>, with each half filament contributing to a distinct half dataset. The box size used are indicated in Supplementary Table 3. Per-particle CTF refinement was performed with FREALIGN<sup>78</sup>.

To select for tubulins bound to kinesin motors and to improve the resolution of the kinesin-tubulin complexes the procedure HSARC<sup>21</sup> was used for these one-head-bound states. The procedure follows these steps:

- (1) Relion helical refinement. The two independent FREALIGN helical refined half datasets were subjected to a single helical refinement in Relion 3.1<sup>79</sup> where each dataset was assigned to a distinct half-set and using as priors the Euler angle values determined in the helical-single-particle 3D reconstruction (initial resolution: 8 Å, sigma on Euler angles sigma\_ang: 1.5, no helical parameter search).
- (2) Asymmetric refinement with partial signal subtraction. An atomic model of a kinesin-tubulin complex was used to generate two soft masks using EMAN pdb2mrc and relion\_mask\_create (low-pass filtration: 30 Å, initial threshold: 0.05, extension: 14 pixels, soft edge: 6 or 8 pixels). One mask (mask<sub>full</sub>)

was generated from a kinesin model bound to one tubulin dimer and two longitudinally flanking tubulin subunits while the other mask (mask<sub>kinesin</sub>) was generated with only the kinesin coordinates. The helical dataset alignment file was symmetry expanded using the 15R microtubule symmetry of the dataset. Partial signal subtraction was then performed using mask<sub>full</sub> to retain the signal within that mask. During this procedure, images were re-centered on the projections of 3D coordinates of the center of mass of mask<sub>full</sub> (C<sub>M</sub>) using a box size as indicated in Supplementary Table 3. The partially signal subtracted dataset was then used in a Relion 3D refinement procedure using as priors the Euler angle values determined from the Relion helical refinement and the symmetry expansion procedure (initial resolution: 8 Å, sigma\_ang: 2, offset range corresponding to 3.5 Å, healpix\_order and auto\_local\_healpix\_order set to 5). The CTF of each particle was corrected to account for their different position along the optical axis.

- (3) 3D classification of the kinesin signal. A second partial signal subtraction procedure identical to the first one but using mask<sub>kinesin</sub> and with particles re-centered on the projections of C<sub>M</sub> was performed to subtract all but the kinesin signal. The images obtained were resampled to 3.5 Å/pixel and the 3D refinement from step 2 was used to update the Euler angles and shifts of all particles. A 3D focused classification without images alignment and using a mask for the kinesin generated like mask<sub>kinesin</sub> was then performed on the resampled dataset (8 classes, tau2\_fudge: 4, padding: 2, iterations: 175). All datasets but MT-CaKip3-MDN-ANP and MT-CaKip3-MDC-AAF classifications produced one major class with a class average where the kinesin motor densities were well-resolved while the others had absent or poorly-resolved kinesin densities. In all cases, only a single motor main domain conformation (open vs. closed) was found per dataset. In case of the two largest datasets (MT-CaKip3-MDN-ANP and MT-CaKip3-MDC-AAF), 2 classes averages had well-resolved densities and the particles belonging to these two classes were merged to generate the average structure. These best classes were selected to generate the average kinesin-tubulin structure in the following step.
- (4) 3D reconstructions with original images (not signal subtracted). To avoid potential artifacts introduced by the signal subtraction procedure, final 3D reconstructions were obtained using relion\_reconstruct on the original image-particles without signal subtraction.

To obtain a final locally filtered and locally sharpened map, post-processing of the pair of unfiltered and unsharpened half maps was performed as follows. One of the two unfiltered half-map was low-pass-filtered to 15 Å and the minimal threshold value that does not show noise around the microtubule fragment was used to generate a mask with relion\_mask\_create (low-pass filtration: 15 Å, extension: 10 pixels, soft edge: 10 pixels). This soft mask was used in blocres<sup>80</sup> on 12-pixel size boxes to obtain initial local resolution estimates. The merged map was locally filtered by blocfilt<sup>80</sup> using blocres local resolution estimates and then used for local low-pass filtration and local sharpening in localdeblur<sup>81</sup> with resolution search up to 25 Å. The localdeblur program converged to a filtration appropriate for the tubulin part of the map but over-sharpened for the kinesin part. The maps at every localdeblur cycle were saved and the maps with better filtration for the kinesin part area, with the aim of resolving better the kinesin loops, were selected.

**Processing of the cryo-EM CT-CaKip3-MDC-ANP dataset.** The frames were aligned with relion implementation of the motioncor2 algorithm. Contrast transfer function (CTF) parameters per micrographs were estimated with Gctf<sup>76</sup> on aligned and non-dose-weighted movie averages. The rest of the processing was done using Relion 3.1<sup>79</sup> unless indicated otherwise.

A first dataset collected with no stage tilt was analyzed with 2D classifications after picking ring-like structures to observe the different structures present. Representative class averages of the different structures that were detected are presented in Supplementary Fig. 4. The samples of CaKip3 mixed with tubulin, dolastatin-10 and AMP-PNP contained both rings of various diameters and spring/spiral-like flexible structures (Supplementary Fig. 4a, b). Because the dolastatin-10 rings have a strong preferential orientation (Supplementary Fig. 4b), the processing to obtain a 3D structure was done on a dataset collected at a 40-degree stage tilt. The flexible spring/spirals-like structures were avoided during the particle picking to focus on the rings. A subset of ~2k rings with a wide range of out of plane tilt were first picked manually. On data resampled to ~4 Å/pix, a series of 3 cycles of 2D classification followed by re-centering on the ring centers was applied to generate the class averages subsequently used as template for automated picking with a low-pass filtration of 50 Å. Using the resulting automatically picked particles, 3 cycles of 2D classification, re-centering, and particle extraction were performed to select rings. The predominant rings type that has 14 asymmetric units (called “C14 rings” from here) was selected. Representative 2D class averages obtained at the end of the third 2D classification are provided in Supplementary Fig. 4c. Local CTF parameters estimation for each of these C14 rings was performed using Gctf. These particles were resampled at 1.5 Å/pixel with 512-pixel box size particle-images and then used in a 3D refinement with C1 symmetry (initial resolution 60 Å) using an initial model generated by ab-initio modeling, with its handedness corrected. A 3D classification on data resampled at ~3.5 Å/pixel (6 classes, tau2\_fudge 2, 25 iterations) was then used to select the rings



contributing to the main class characterized by the most regular ring structure (71% of the particles). A 3D refinement was then performed with a C1 symmetry, the initial model mentioned above low-pass filtered at 30 Å and without mask. Duplicated particles were then removed, leading to ~38 k C14 rings (Table 2). No further particle classification was used from that stage of the processing, with a homogeneous set of C14 rings. A 3D refinement with C14 symmetry was then performed with an initial resolution of 20 Å, a soft mask around the ring (from the previous map with `reliion_mask_create`: low-pass filtration 30 Å, threshold 0.01, extension 25 pixels, soft edge 10 pixels), the `solvent_correct_fsc` option and local constrains (`offset_range` 2, `offset_step` 1, `sigma_ang` 2) and led a 6.2 Å map of the full ring structure. A CTF refinement step using only brute-force defocus search over a scan range of 3000 Å was performed followed by a 3D refinement with identical parameters as the previous one, which improved the resolution to 5.1 Å. A step of particle polishing (with box size of 700 pixels and scaled down to 512 pixels, 1.5 Å/pixel) without training and followed by a 3D refinement (initial resolution 10 Å, a soft mask around the ring made as before, with the `solvent_correct_fsc` option and local constrains `offset_range` 2, `offset_step` 1 & `sigma_ang` 2) enabled to improve the resolution to 4.8 Å. Repeating the previous polishing and 3D refinements steps led to a 4.7 Å map at 1.5 Å/pixel. These 2 cycles of particles polishing followed by 3D refinements were repeated without binning the data (box size 700 pixels, 1.083 Å/pixel), this time with local constrains `offset_range` 6 and `sigma_ang` 5 and led to a full scale C14 ring map at 4.5 Å. A third cycle didn't improve the resolution and led to the final full C14 ring map (Fig. 1a).

The processing was continued by doing local alignments focused on fragments of the C14 rings as described in the following. First, to continue the processing locally without losing the benefit from the particle polishing done on the full rings, the polished particles from the previous polishing step were regenerated on larger 900-pixel boxes. Symmetry expansion of the last alignment data based on the C14 symmetry was followed by a `reliion` particle extraction step using the 900 pixels size polished particles-images as input and with re-centering on the center of a mask covering a single asymmetric unit. This enabled to extract from each of these C14 rings in 900-pixel boxes, 14 particles each in 416-pixel boxes and each centered on a different asymmetric unit, for a total of ~531k particles (Table 2). The defocus of these particles was updated, considering their different position along the optical axis. A preliminary PDB was used to create with EMAN `pdb2mrc` and `reliion_mask_create` a soft mask covering 3 asymmetric units (low-pass filtration 30 Å, initial threshold 0.3, extension 30 pixels, soft edge 6 Å). That mask was used in a focused refinement with fixed priors on the Euler angles and shifts based on the previous alignment data, local constrains (`offset_range` 6, `offset_step` 1, `sigma_ang` 5) and started with the reconstruction of this expanded data filtered at 10 Å. This focused refinement produced a 4.0 Å map (Fig. 1f, top structure). Repeating the same focused refinement but with a mask made similarly covering only the central asymmetric unit (low-pass filtration 30 Å, initial threshold 0.3, extension 20 pixels, soft edge 6 Å) and with tighter local constrains (`offset_range` 3, `offset_step` 1, `sigma_ang` 2) produced a 3.9 Å map. To obtain a final locally filtered and locally sharpened map, the same procedure as the one used for the microtubule datasets was used, leading to the final map (Fig. 1f, bottom structure).

**Cryo-EM resolution estimation.** The final resolutions for each cryo-EM reconstruction were estimated from FSC curves generated with Relion 3.1 postprocess ( $FSC_{0.143}$  criteria, Table 2, Supplementary Fig. 3). To estimate the overall resolution, these curves were computed from the two independently refined half maps (gold standard) using soft masks that isolate a single asymmetric unit containing a kinesin and a tubulin dimer. The soft masks were created with Relion 3.1 `reliion_mask_create` (for microtubule datasets: low-pass filtration: 15 Å, threshold: 0.1, extension: 2 pixels, soft edge: 5–6 pixels; for the CT-CaKip3-MDC-ANP dataset: low-pass filtration: 20 Å, threshold: 0.1, extension: 4 pixels, soft edge: 10 pixels) applied on the correctly positioned EMAN `pdb2mrc` density map generated with the coordinates of the respective refined atomic models. FSC curves for the tubulin or kinesin parts of the maps were generated similarly using the corresponding subset of the PDB model to mask only a kinesin or a tubulin dimer (Supplementary Fig. 3, Table 2).

The final cryo-EM maps together with the corresponding half maps, masks used for resolution estimation, masks used in the partial signal subtraction for the microtubule datasets, and the FSC curves are deposited in the Electron Microscopy Data Bank (Table 2).

**Model building from cryo-EM densities.** Atomic models of the cryo-EM density maps were built as follow. First, atomic models for the kinesin chains were generated from their amino-acid sequence by homology modeling using Modeler<sup>82</sup>. The initial tubulin structures were taken from<sup>21</sup>. Second, the protein chains were manually placed into the cryo-EM densities and fitted as rigid bodies using UCSF-Chimera<sup>83</sup>. Third, the models were flexibly fitted into the density maps using Rosetta for cryo-EM relax protocols<sup>84,85</sup> and the models with the best scores (best match to the cryo-EM density and best molprobity scores) were selected. Fourth, the Rosetta-refined models were further refined against the cryo-EM density maps using PHENIX real space refinement tools<sup>70</sup> and/or ISOLDE<sup>86</sup>. Fifth, the models were edited using Coot<sup>69</sup>. Several iterations of Phenix real space refinement and Coot editing were performed to reach the final atomic models. Atomic models and cryo-EM map figures were prepared with UCSF-Chimera<sup>83</sup> and ChimeraX<sup>87</sup>.

**Reporting summary.** Further information on research design is available in the Nature Research Reporting Summary linked to this article.

## Data availability

Atomic coordinates of the CaKip3-MDN-ADP X-ray crystal structure have been deposited in the Protein Data Bank (PDB) under accession code 7LFF (Table 1). Atomic coordinates and corresponding cryo-EM density maps, including the half maps, masks and FSC curves used to estimate spatial resolution have been deposited in the Protein Data Bank (PDB) and Electron Microscopy Data Bank (EMDB) under the accession codes 7TQX, 7TQY, 7TQZ, 7TR0, 7TR1, 7TR2, 7TR3, and EMD-26074, EMD-26075, EMD-26076, EMD-26077, EMD-26078, EMD-26079, EMD-26080 (Table 2). Source data are provided with this paper.

Received: 26 May 2022; Accepted: 4 July 2022;

Published online: 20 July 2022

## References

- Gupta, M. L. Jr., Carvalho, P., Roof, D. M. & Pellman, D. Plus end-specific depolymerase activity of Kip3, a kinesin-8 protein, explains its role in positioning the yeast mitotic spindle. *Nat. Cell Biol.* **8**, 913–923 (2006).
- Varga, V. et al. Yeast kinesin-8 depolymerizes microtubules in a length-dependent manner. *Nat. Cell Biol.* **8**, 957–962 (2006).
- Mayr, M. I. et al. The human kinesin Kif18A is a motile microtubule depolymerase essential for chromosome congression. *Curr. Biol.* **17**, 488–498 (2007).
- Varga, V., Leduc, C., Bormuth, V., Diez, S. & Howard, J. Kinesin-8 motors act cooperatively to mediate length-dependent microtubule depolymerization. *Cell* **138**, 1174–1183 (2009).
- McHugh, T., Gluszek, A. A. & Welburn, J. P. Microtubule end tethering of a processive kinesin-8 motor Kif18b is required for spindle positioning. *J. Cell Biol.* **217**, 2403–2416 (2018). in.
- Tanenbaum, M. E. et al. A complex of Kif18b and MCAK promotes microtubule depolymerization and is negatively regulated by Aurora kinases. *Curr. Biol.* **21**, 1356–1365 (2011).
- Grissom, P. M. et al. Kinesin-8 from fission yeast: a heterodimeric, plus-end-directed motor that can couple microtubule depolymerization to cargo movement. *Mol. Biol. Cell* **20**, 963–972 (2009).
- DeZwaan, T. M., Ellingson, E., Pellman, D. & Roof, D. M. Kinesin-related KIP3 of *Saccharomyces cerevisiae* is required for a distinct step in nuclear migration. *J. Cell Biol.* **138**, 1023–1040 (1997).
- Stumpff, J., von Dassow, G., Wagenbach, M., Asbury, C. & Wordeman, L. The kinesin-8 motor Kif18A suppresses kinetochore movements to control mitotic chromosome alignment. *Dev. Cell* **14**, 252–262 (2008).
- Straight, A. F., Sedat, J. W. & Murray, A. W. Time-lapse microscopy reveals unique roles for kinesins during anaphase in budding yeast. *J. Cell Biol.* **143**, 687–694 (1998).
- Unsworth, A., Masuda, H., Dhut, S. & Toda, T. Fission yeast kinesin-8 Klp5 and Klp6 are interdependent for mitotic nuclear retention and required for proper microtubule dynamics. *Mol. Biol. Cell* **19**, 5104–5115 (2008).
- Savoian, M. S. & Glover, D. M. *Drosophila* Klp67A binds prophase kinetochores to subsequently regulate congression and spindle length. *J. Cell Sci.* **123**, 767–776 (2010).
- Wargacki, M. M., Tay, J. C., Muller, E. G., Asbury, C. L. & Davis, T. N. Kip3, the yeast kinesin-8, is required for clustering of kinetochores at metaphase. *Cell Cycle* **9**, 2581–2588 (2010).
- Goshima, K. & Vale, R. D. Cell cycle-dependent dynamics and regulation of mitotic kinesins in *Drosophila* S2 cells. *Mol. Biol. Cell* **16**, 3896–3907 (2005).
- Rizk, R. S., Discipio, K. A., Proudfoot, K. G. & Gupta, M. L. Jr. The kinesin-8 Kip3 scales anaphase spindle length by suppression of midzone microtubule polymerization. *J. Cell Biol.* **204**, 965–975 (2014).
- Walczak, C. E., Zong, H., Jain, S. & Stout, J. R. Spatial regulation of astral microtubule dynamics by Kif18B in PtK cells. *Mol. Biol. Cell* **27**, 3021–3030 (2016).
- Weaver, L. N. et al. Kif18A uses a microtubule binding site in the tail for plus-end localization and spindle length regulation. *Curr. Biol.* **21**, 1500–1506 (2011).
- Su, X. et al. Mechanisms underlying the dual-mode regulation of microtubule dynamics by Kip3/kinesin-8. *Mol. Cell* **43**, 751–763 (2011).
- McHugh, T. & Welburn, J.P.I. Potent microtubule depolymerizing activity of a mitotic Kif18b-MCAK-EB network. *J. Cell Sci.* **136**, jcs260144 (2022).
- Atherton, J. et al. Conserved mechanisms of microtubule-stimulated ADP release, ATP binding, and force generation in transport kinesins. *Elife* **3**, e03680 (2014).

21. Benoit, M. et al. Structural basis of mechano-chemical coupling by the mitotic kinesin KIF14. *Nat. Commun.* **12**, 3637 (2021).
22. Shang, Z. et al. High-resolution structures of kinesin on microtubules provide a basis for nucleotide-gated force-generation. *Elife* **3**, e04686 (2014).
23. Helenius, J., Brouhard, G., Kalaidzidis, Y., Diez, S. & Howard, J. The depolymerizing kinesin MCAK uses lattice diffusion to rapidly target microtubule ends. *Nature* **441**, 115–119 (2006).
24. Benoit, M., Asenjo, A. B. & Sosa, H. Cryo-EM reveals the structural basis of microtubule depolymerization by kinesin-13s. *Nat. Commun.* **9**, 1662 (2018).
25. Wang, W. et al. Insight into microtubule disassembly by kinesin-13s from the structure of Kif2C bound to tubulin. *Nat. Commun.* **8**, 70 (2017).
26. Asenjo, A. B. et al. Structural model for tubulin recognition and deformation by kinesin-13 microtubule depolymerases. *Cell Rep.* **3**, 759–768 (2013).
27. Trofimova, D. et al. Ternary complex of Kif2A-bound tandem tubulin heterodimers represents a kinesin-13-mediated microtubule depolymerization reaction intermediate. *Nat. Commun.* **9**, 2628 (2018).
28. Arellano-Santoyo, H. et al. A tubulin binding switch underlies Kip3/kinesin-8 depolymerase activity. *Dev. Cell* **42**, 37–51 e8 (2017).
29. Arellano-Santoyo, H. et al. Multimodal tubulin binding by the yeast kinesin-8, Kip3, underlies its motility and depolymerization. Preprint at *bioRxiv* <https://doi.org/10.1101/2021.10.12.464151> (2021).
30. Locke, J. et al. Structural basis of human kinesin-8 function and inhibition. *Proc. Natl Acad. Sci. USA* **114**, E9539–E9548 (2017).
31. Peters, C. et al. Insight into the molecular mechanism of the multitasking kinesin-8 motor. *EMBO J.* **29**, 3437–3447 (2010).
32. Wang, D. et al. Motility and microtubule depolymerization mechanisms of the Kinesin-8 motor, KIF19A. *Elife* **5**, e18101 (2016).
33. Bachewich, C., Nantel, A. & Whiteway, M. Cell cycle arrest during S or M phase generates polarized growth via distinct signals in *Candida albicans*. *Mol. Microbiol.* **57**, 942–959 (2005).
34. Cottingham, F. R. & Hoyt, M. A. Mitotic spindle positioning in *Saccharomyces cerevisiae* is accomplished by antagonistically acting microtubule motor proteins. *J. Cell Biol.* **138**, 1041–1053 (1997).
35. West, R. R., Malmstrom, T. & McIntosh, J. R. Kinesins klp5(+) and klp6(+) are required for normal chromosome movement in mitosis. *J. Cell Sci.* **115**, 931–940 (2002).
36. Garcia, M. A., Koonrugsa, N. & Toda, T. Two kinesin-like Kin I family proteins in fission yeast regulate the establishment of metaphase and the onset of anaphase A. *Curr. Biol.* **12**, 610–621 (2002).
37. Goshima, G. & Vale, R. D. The roles of microtubule-based motor proteins in mitosis: comprehensive RNAi analysis in the *Drosophila* S2 cell line. *J. Cell Biol.* **162**, 1003–1016 (2003).
38. Gandhi, R. et al. The *Drosophila* kinesin-like protein KLP67A is essential for mitotic and male meiotic spindle assembly. *Mol. Biol. Cell* **15**, 121–131 (2004).
39. Goshima, G., Wollman, R., Stuurman, N., Scholey, J. M. & Vale, R. D. Length control of the metaphase spindle. *Curr. Biol.* **15**, 1979–1988 (2005).
40. Wang, H., Brust-Mascher, I., Cheerambathur, D. & Scholey, J. M. Coupling between microtubule sliding, plus-end growth and spindle length revealed by kinesin-8 depletion. *Cytoskeleton (Hoboken)* **67**, 715–728 (2010).
41. Stout, J. R. et al. Kif18B interacts with EB1 and controls astral microtubule length during mitosis. *Mol. Biol. Cell* **22**, 3070–3080 (2011).
42. McCoy, K. M. et al. Physical limits on kinesin-5-mediated chromosome congression in the smallest mitotic spindles. *Mol. Biol. Cell* **26**, 3999–4014 (2015).
43. Moores, C. A. & Milligan, R. A. Visualisation of a kinesin-13 motor on microtubule end mimics. *J. Mol. Biol.* **377**, 647–654 (2008).
44. Kikkawa, M. & Hirokawa, N. High-resolution cryo-EM maps show the nucleotide binding pocket of KIF1A in open and closed conformations. *EMBO J.* **25**, 4187–4194 (2006).
45. Kikkawa, M. et al. Switch-based mechanism of kinesin motors. *Nature* **411**, 439–445 (2001).
46. Sindelar, C. V. & Downing, K. H. An atomic-level mechanism for activation of the kinesin molecular motors. *Proc. Natl Acad. Sci. USA* **107**, 4111–4116 (2010).
47. Ogawa, T., Nitta, R., Okada, Y. & Hirokawa, N. A common mechanism for microtubule destabilizers-M type kinesins stabilize curling of the protofilament using the class-specific neck and loops. *Cell* **116**, 591–602 (2004).
48. Tan, D., Rice, W. J. & Sosa, H. Structure of the kinesin13-microtubule ring complex. *Structure* **16**, 1732–1739 (2008).
49. Wang, W. et al. New insights into the coupling between microtubule depolymerization and ATP hydrolysis by kinesin-13 protein Kif2C. *J. Biol. Chem.* **290**, 18721–18731 (2015).
50. Cao, L. et al. The structure of apo-kinesin bound to tubulin links the nucleotide cycle to movement. *Nat. Commun.* **5**, 5364 (2014).
51. Gigant, B. et al. Structure of a kinesin-tubulin complex and implications for kinesin motility. *Nat. Struct. Mol. Biol.* **20**, 1001–1007 (2013).
52. Gigant, B. et al. The 4 A X-ray structure of a tubulin:stathmin-like domain complex. *Cell* **102**, 809–816 (2000).
53. Nawrotek, A., Knossow, M. & Gigant, B. The determinants that govern microtubule assembly from the atomic structure of GTP-tubulin. *J. Mol. Biol.* **412**, 35–42 (2011).
54. Shipley, K. et al. Structure of a kinesin microtubule depolymerization machine. *EMBO J.* **23**, 1422–1432 (2004).
55. Bell, K. M., Cha, H. K., Sindelar, C. V. & Cochran, J. C. The yeast kinesin-5 Cin8 interacts with the microtubule in a noncanonical manner. *J. Biol. Chem.* **292**, 14680–14694 (2017).
56. Walther, A. & Wendland, J. An improved transformation protocol for the human fungal pathogen *Candida albicans*. *Curr. Genet.* **42**, 339–343 (2003).
57. Frazer, C. et al. *Candida albicans* kinesin Kar3 depends on a Cik1-like regulatory partner protein for its roles in mating, cell morphogenesis, and bipolar spindle formation. *Eukaryot. Cell* **14**, 755–774 (2015).
58. Noble, S. M. & Johnson, A. D. Strains and strategies for large-scale gene deletion studies of the diploid human fungal pathogen *Candida albicans*. *Eukaryot. Cell* **4**, 298–309 (2005).
59. Shoukat, I., Frazer, C. & Allingham, J. S. Kinesin-5 is dispensable for bipolar spindle formation and elongation in *Candida albicans*, but simultaneous loss of kinesin-14 activity is lethal. *mSphere* **4**, e00610-19 (2019).
60. Castoldi, M. & Popov, A. V. Purification of brain tubulin through two cycles of polymerization-depolymerization in a high-molarity buffer. *Protein Expr. Purif.* **32**, 83–88 (2003).
61. Arora, K. et al. KIF14 binds tightly to microtubules and adopts a rigor-like conformation. *J. Mol. Biol.* **426**, 2997–3015 (2014).
62. Duan, D., Hnatchuk, D. J., Brenner, J., Davis, D. & Allingham, J. S. Crystal structure of the Kar3-like kinesin motor domain from the filamentous fungus *Ashbya gossypii*. *Proteins* **80**, 1016–1027 (2012).
63. Huang, T. G. & Hackney, D. D. *Drosophila* kinesin minimal motor domain expressed in *Escherichia coli*. Purification and kinetic characterization. *J. Biol. Chem.* **269**, 16493–16501 (1994).
64. Mulder, A. M. et al. A new model for binding of kinesin 13 to curved microtubule protofilaments. *J. Cell Biol.* **185**, 51–57 (2009).
65. Duan, D. et al. Neck rotation and neck mimic docking in the noncatalytic Kar3-associated protein Vik1. *J. Biol. Chem.* **287**, 40292–40301 (2012).
66. Sridhar, P. S. et al. Ste2 receptor-mediated chemotropism of *Fusarium graminearum* contributes to its pathogenicity against wheat. *Sci. Rep.* **10**, 10770 (2020).
67. Kabsch, W. XDS. *Acta Crystallogr. Sect. D, Biol. Crystallogr.* **66**, 125–132 (2010).
68. Vagin, A. & Teplyakov, A. An approach to multi-copy search in molecular replacement. *Acta Crystallogr. D. Biol. Crystallogr.* **56**, 1622–1624 (2000).
69. Emsley, P. & Cowtan, K. Coot: model-building tools for molecular graphics. *Acta Crystallogr. D. Biol. Crystallogr.* **60**, 2126–2132 (2004).
70. Adams, P. D. et al. PHENIX: a comprehensive Python-based system for macromolecular structure solution. *Acta Crystallogr. D. Biol. Crystallogr.* **66**, 213–221 (2010).
71. Suloway, C. et al. Automated molecular microscopy: the new Legion system. *J. Struct. Biol.* **151**, 41–60 (2005).
72. Glaeser, R. M., Typke, D., Tiemeijer, P. C., Pulokas, J. & Cheng, A. Precise beam-tilt alignment and collimation are required to minimize the phase error associated with coma in high-resolution cryo-EM. *J. Struct. Biol.* **174**, 1–10 (2011).
73. Tan, Y. Z. et al. Addressing preferred specimen orientation in single-particle cryo-EM through tilting. *Nat. Methods* **14**, 793–796 (2017).
74. Zheng, S. Q. et al. MotionCor2: anisotropic correction of beam-induced motion for improved cryo-electron microscopy. *Nat. Methods* **14**, 331–332 (2017).
75. Grant, T. & Grigorieff, N. Automatic estimation and correction of anisotropic magnification distortion in electron microscopes. *J. Struct. Biol.* **192**, 204–208 (2015).
76. Zhang, K. Gctf: Real-time CTF determination and correction. *J. Struct. Biol.* **193**, 1–12 (2016).
77. Grigorieff, N. FREALIGN: An Exploratory Tool for Single-Particle Cryo-EM. *Methods Enzymol.* **579**, 191–226 (2016).
78. Grant, T., Rohou, A. & Grigorieff, N. cisTEM, user-friendly software for single-particle image processing. *Elife* **7**, e35383 (2018).
79. Zivanov, J. et al. New tools for automated high-resolution cryo-EM structure determination in RELION-3. *Elife* **7**, e42166 (2018).
80. Heymann, J. B. & Belnap, D. M. Bsoft: image processing and molecular modeling for electron microscopy. *J. Struct. Biol.* **157**, 3–18 (2007).
81. Ramirez-Aportela, E. et al. Automatic local resolution-based sharpening of cryo-EM maps. *Bioinformatics* **36**, 765–772 (2020).
82. Fiser, A. & Sali, A. Modeller: generation and refinement of homology-based protein structure models. *Methods Enzymol.* **374**, 461–491 (2003).
83. Pettersen, E. F. et al. UCSF Chimera—a visualization system for exploratory research and analysis. *J. Comput. Chem.* **25**, 1605–1612 (2004).
84. DiMaio, F., Tyka, M. D., Baker, M. L., Chiu, W. & Baker, D. Refinement of protein structures into low-resolution density maps using rosetta. *J. Mol. Biol.* **392**, 181–190 (2009).

85. Wang, R. Y. et al. De novo protein structure determination from near-atomic-resolution cryo-EM maps. *Nat. Methods* **12**, 335–338 (2015).
86. Croll, T. I. ISOLDE: a physically realistic environment for model building into low-resolution electron-density maps. *Acta Crystallogr. D. Struct. Biol.* **74**, 519–530 (2018).
87. Goddard, T. D. et al. UCSF ChimeraX: meeting modern challenges in visualization and analysis. *Protein Sci.* **27**, 14–25 (2018).

### Acknowledgements

This work was supported by Canadian Institutes of Health Research Grant PJT-169149 (J.S.A.), National Sciences and Engineering Council of Canada grant RGPIN-2019-05924 (J.S.A.), and National Institutes of Health Grant R01GM113164 (H.S.). Cryo-EM data collection was performed at the Simons Electron Microscopy Center (SEMC) and National Resource for Automated Molecular Microscopy located at the New York Structural Biology Center, supported by grants from the Simons Foundation (SF349247), NYSTAR, and the NIH National Institute of General Medical Sciences (GM103310) with additional support from Agouron Institute (F00316) and NIH (OD019994). We thank Peter Davies for the use of his Olympus IX83 inverted fluorescence microscope. We thank Huihui Kuang, Daija Bobe, Carolina Hernandez, Kashyap Maruthi, Kasahun Neselu and Mykhailo Kopylov for assistance and support during data collection at SEMC. B.H. is an NSERC Canada Graduate Scholarship and Ontario Graduate Scholarship recipient.

### Author contributions

B.H., C.F., and I.S. constructed the *wild type* and *kip3* mutant *Candida albicans* strains used to understand CaKip3 protein functions in vivo. B.H., C.F., and I.S. conducted the cell growth, cell imaging, and phenotypic analysis of these strains. B.H., C.D., and D.T. cloned, expressed, and purified the kinesin proteins; B.H. and J.S.A. collected X-ray diffraction data for the CaKip3-MDN crystal, determined the structure, built and refined the atomic model, and analyzed the structure; M.P.M.H.B. and A.B.A. assembled kinesin-microtubule and kinesin-curved tubulin complexes and made cryo-EM grid samples; A.B.A. performed sample screening and optimization for cryo-EM imaging and performed microtubule selection; M.P.M.H.B. and A.B.A. designed the cryo-EM experiments and performed cryo-EM data collection; M.P.M.H.B. designed and performed the cryo-EM data processing of kinesin-microtubule and kinesin-ring complexes, mechanistically interpreted the cryo-EM structures and proposed several of the biochemical experiments; M.P.M.H.B. and H.S. built and refined the atomic models, and analyzed the

structures; B.H. designed the biochemical analyses; B.H. and C.D. performed ATPase assays; B.H. performed all other biochemical experiments; J.S.A. and H.S. supervised the project; B.H., M.P.M.H.B., A.B.A., H.S., and J.S.A. wrote the manuscript.

### Competing interests

The authors declare no competing interests.

### Additional information

**Supplementary information** The online version contains supplementary material available at <https://doi.org/10.1038/s41467-022-31794-3>.

**Correspondence** and requests for materials should be addressed to Hernando Sosa or John S. Allingham.

**Peer review information** *Nature Communications* thanks the other, anonymous, reviewer(s) for their contribution to the peer review of this work.

**Reprints and permission information** is available at <http://www.nature.com/reprints>

**Publisher's note** Springer Nature remains neutral with regard to jurisdictional claims in published maps and institutional affiliations.



**Open Access** This article is licensed under a Creative Commons Attribution 4.0 International License, which permits use, sharing, adaptation, distribution and reproduction in any medium or format, as long as you give appropriate credit to the original author(s) and the source, provide a link to the Creative Commons license, and indicate if changes were made. The images or other third party material in this article are included in the article's Creative Commons license, unless indicated otherwise in a credit line to the material. If material is not included in the article's Creative Commons license and your intended use is not permitted by statutory regulation or exceeds the permitted use, you will need to obtain permission directly from the copyright holder. To view a copy of this license, visit <http://creativecommons.org/licenses/by/4.0/>.

© The Author(s) 2022